Geochemistry, Geophysics, Geosystems®

AGU ADVANCING EARTH AND SPACE SCIENCES

RESEARCH ARTICLE
10.1029/2025GC012419

Soil Gas Investigations in Hatay-Reyhanlı (Türkiye): Implications for Buried Fault Detection and Seismic Hazard Assessment

G. Yüce[1,2], C. C. Fu[3], W. D'Alessandro[2], B. Kahraman[1], B. Kürkcüoglu[1], F. Italiano[4,5], A. H. Gülbay[6], H. Elmacı[7], M. İçhedef[8], A. Özdemir[1], H. Akıllı[9], D. Yasin[10], Ş. Gürboğa[11], A. Demirtaş[1], L. H. Lin[12], P. L. Wang[13], and S. Över[14]

[1]Department of Geological Engineering, Hydrogeology Division, Hacettepe University, Ankara, Türkiye, [2]Istituto Nazionale di Geofisica e Vulcanologia (INGV), Palermo, Italy, [3]Academia Sinica, Institute of Earth Sciences, Taipei, Taiwan, [4]OGS, Sgonico, Italy, [5]Athanor-Geotech srls, Rome, Italy, [6]Koza Gold Cooperation, Ankara, Türkiye, [7]Department of Geological Research, General Directorate of Mineral Research and Exploration (MTA), Ankara, Turkiye, [8]Ege University, Institute of Nuclear Sciences, Izmir, Türkiye, [9]General Directorate of Mineral Research and Exploration, Occupational Health and Safety Coordination, Ankara, Türkiye, [10]Department of Geological Engineering, Eskişehir Osmangazi University, Eskişehir, Türkiye, [11]Department of Geological Engineering, Faculty of Mines, İstanbul Technical University, İstanbul, Türkiye, [12]Department of Geosciences, National Taiwan University, Taipei, Taiwan, [13]Institute of Oceanography, National Taiwan University, Taipei, Taiwan, [14]Department of Civil Engineering, İskenderun Technical University, Hatay, Türkiye

Key Points:

- Soil gas surveys identified concealed fault zones near Reyhanlı Dam and central Reyhanlı through CO_2 and radon anomalies
- Isotope data confirmed deep crustal gas sources and fault-controlled vertical migration in the Hatay region
- CO_2 emissions from the Amik Basin contribute significantly to natural degassing, with implications for seismic hazard mapping

Correspondence to:
C. C. Fu,
ccfu@earth.sinica.edu.tw

Citation:
Yüce, G., Fu, C. C., D'Alessandro, W., Kahraman, B., Kürkcüoglu, B., Italiano, F., et al. (2026). Soil gas investigations in Hatay-Reyhanlı (Türkiye): Implications for buried Fault detection and seismic hazard assessment. *Geochemistry, Geophysics, Geosystems*, *27*, e2025GC012419. https://doi.org/10.1029/2025GC012419

Received 5 MAY 2025
Accepted 21 DEC 2025
Corrected 14 FEB 2026

This article was corrected on 14 FEB 2026. See the end of the full text for details.

Author Contributions:
Conceptualization: G. Yüce, C. C. Fu
Data curation: C. C. Fu, B. Kahraman, B. Kürkcüoglu, A. H. Gülbay, H. Elmacı, M. İçhedef, A. Özdemir, H. Akıllı, D. Yasin, Ş. Gürboğa, A. Demirtaş
Funding acquisition: G. Yüce, C. C. Fu
Investigation: G. Yüce, C. C. Fu, W. D'Alessandro, B. Kahraman, B. Kürkcüoglu, F. Italiano, A. H. Gülbay, H. Elmacı, M. İçhedef, A. Özdemir, H. Akıllı, A. Demirtaş
Methodology: C. C. Fu, W. D'Alessandro, F. Italiano
Project administration: G. Yüce

Abstract This study presents a soil gas geochemical survey in the Kırcaoğlu and Reyhanlı regions of Hatay Province, southeastern Türkiye, following the 2023 Kahramanmaraş earthquake doublet. The aim was to identify concealed faults and assess seismic hazard through analysis of soil CO_2 flux, CO_2 and ^{222}Rn concentrations, and carbon and helium isotopic compositions. A total of 98 sites were surveyed, and graphical statistical methods were used to establish geochemical anomaly thresholds. In Kırcaoğlu, two prominent gas anomaly zones were delineated with dominant NW-SE and NE-SW trends, likely representing buried faults linked to the Yesemek Segment, including one beneath the Reyhanlı Dam. In Reyhanlı, an east-west gas anomaly suggests a possible westward extension of the Reyhanlı Fault. These findings refine the region's structural framework and highlight seismic risks from buried faults. Isotopic analyses show CO_2 derives from biogenic and deep crustal reservoirs, with $^4He/^{20}Ne$ and $^3He/^4He$ ratios confirming up to 7.1% crustal helium and <1% mantle helium. Heavier $\delta^{13}C$ values and elevated crustal helium in Kırcaoğlu support deep gas migration along fault zones. Natural CO_2 emissions are estimated at 66 t/d in Kırcaoğlu and 60 t/d in Reyhanlı. Regionally, emissions from the Amik Basin (~15,586 t/d) comprise ~1.5% of Türkiye's daily anthropogenic CO_2. The overlap between gas anomalies and surface ruptures and liquefaction zones from the 2023 earthquakes confirms the effectiveness of soil gas surveys for buried fault detection. These results highlight the utility of soil gas geochemistry as a non-invasive tool for fault detection and seismic hazard assessment.

Plain Language Summary In this study, scientists examined soil gases in the Kırcaoğlu and Reyhanlı regions of Hatay Province, southeastern Türkiye, after the 2023 earthquakes. The goal was to better understand hidden faults underground that could cause future earthquakes. CO_2 and Rn gases were measured at 98 sites using specialized equipment. Two areas showed unusual gas patterns. In Kırcaoğlu, gas was leaking along two narrow subsurface paths, likely linked to the Yesemek Segment fault. One of these paths passes beneath the Reyhanlı Dam. In Reyhanlı, the gas distribution indicated that the local fault might extend farther west than previously believed. The gases came from surface biological activity and deep underground sources. The presence of deep gases, especially in Kırcaoğlu, suggests that these faults may allow gases to rise from the Earth's crust. This helps in assessing earthquake risk. The CO_2 emissions from both areas are significant and contribute to Türkiye's natural greenhouse gases. Notably, gas patterns corresponded with areas damaged by the 2023 quakes, including surface ruptures and soil liquefaction. This confirms that soil gas studies can help detect buried faults. Researchers suggest that soil gas monitoring can improve earthquake hazard assessments in densely populated regions and places with critical infrastructure.

Resources: C. C. Fu, L. H. Lin, P. L. Wang
Software: C. C. Fu
Supervision: C. C. Fu
Writing – original draft: G. Yüce, C. C. Fu
Writing – review & editing: W. D'Alessandro, B. Kahraman, B. Kürkcüoglu, F. Italiano, H. Elmacı, M. İçhedef, D. Yasin, Ş. Gürboğa, L. H. Lin, P. L. Wang, S. Över

1. Introduction

Earthquakes rank among the most destructive natural disasters, often resulting in widespread devastation and significant loss of life. Identifying and monitoring active fault lines, especially those invisible at the surface, is essential for assessing earthquake risks and implementing effective mitigation strategies. Terrestrial degassing is a continuous geological process governed primarily by the nature of gas sources, migration pathways, and driving mechanisms. Deep-sourced gases, originating from the crust and upper mantle, commonly ascend through structurally weak zones in the lithosphere (e.g., active faults, plate boundaries, and hot springs) before being released into the atmosphere, which serves as a preferential conduit for gas transport (e.g., D'Alessandro et al., 2020; Hu et al., 2025). Near the surface, soil gases typically exhibit signatures resulting from the mixing of shallow and deep sources. Variations in their composition and flux reflect the complex coupling between internal geodynamic processes and the mechanisms governing degassing at the Earth's surface. In faulted and fractured zones, deep gases such as carbon dioxide (CO_2), helium (He), and radon (^{222}Rn) can migrate upward, often accumulating in shallow strata and producing localized anomalies in soil gas concentrations and fluxes. These anomalies serve as valuable indicators of subsurface fractures and active faults. Elevated concentrations of these gases may indicate the presence of concealed or unmapped fault structures. Such anomalies have been widely employed for the identification and monitoring of fault systems, making them crucial tools for seismic studies (Annunziatellis et al., 2008; Caracausi et al., 2023; Doğan et al., 2009; Fu et al., 2005, 2008, 2025; Fu, Yang, Chen, et al., 2017; Li et al., 2024; Z. Liu et al., 2024; Walia et al., 2005, 2010; Y. Wang et al., 2023, J. Wang et al., 2024; Yuce et al., 2017).

Moreover, seismic activity may induce rock fracturing, thereby increasing subsurface porosity and permeability, which facilitates gas release and fluid migration. Changes in soil gas composition and fluxes have therefore emerged as valuable indicators for assessing fault activity. In summary, gas geochemistry has become a powerful and promising tool for investigating tectonic processes and evaluating seismic hazards (Chiodini et al., 2020; Ciotoli et al., 2014; Cui et al., 2024; D'Alessandro et al., 2020; Girault et al., 2018; Fu & Lee, 2018; Fu et al., 2008; Fu, Yang, Tsai, et al., 2017; Walia et al., 2013; Yang et al., 2006). Notably, between 2013 and 2014, Yuce et al. (2017) conducted a detailed soil gas survey across the Amik Basin in Hatay Province. Their results revealed that anomalous gas emissions spatially coincided with areas of surface rupture and soil liquefaction caused by the 6 February 2023 earthquake (Kürçer, Domaç Yalçın, et al., 2025; Kürçer, Elmacı, et al., 2025; Taftsoglou et al., 2023). Therefore, the current study was conducted to investigate the post-2023 earthquake conditions of the high-anomaly points previously identified in soil-gas radon and CO_2 measurements carried out in the Reyhanlı region (Yuce et al., 2017) and to obtain data with improved resolution. These findings underscore the value of soil gas geochemistry as a tool for detecting hidden fault structures and enhancing seismic hazard assessments.

This approach is especially relevant in earthquake-prone regions such as Osmaniye Province in Türkiye, which is situated along tectonically active zones, and for this reason, the study was extended to include this area. On 6 February 2023, two devastating earthquakes with magnitudes of Mw 7.8 and Mw 7.6 struck the border region between Türkiye and Syria (Dal Zilio & Ampuero, 2023). Collectively referred to as the Kahramanmaraş earthquake doublet, the mainshock ruptured along the East Anatolian Fault (EAF), while the subsequent event propagated toward the Cardak Fault (CF), a subsidiary branch of the EAF (Figure 1). These events resulted in widespread destruction and significant casualties (Erdik et al., 2023). The earthquake sequence comprised six kinematically related sub-events, revealing complex rupture dynamics and stress transfer mechanisms (Barbot et al., 2023; Jia et al., 2023).

Studies on static Coulomb stress changes induced by both historical earthquakes and the 2023 sequence have demonstrated the critical role of pre-existing stress accumulation in rupture initiation. This pre-existing stress has been suggested to contribute to stress loading and the triggering of rupture in specific fault segments (Carena et al., 2023; Chen et al., 2024; Ragon et al., 2021). These earthquakes, among the most powerful ever recorded in the region's history, underscored the seismic hazards associated with the EAF, which is a complex tectonic boundary between the Arabian Plate and the Anatolian Plate.

In the aftermath of the 2023 earthquakes, soil gas measurement studies were conducted to detect buried faults and fracture lines along active fault segments that may potentially rupture in the future due to stress transfer. The research primarily focused on the YS of the EAF zone (Kürçer, Domaç Yalçın, et al., 2025; Kürçer, Elmacı, et al., 2025) and the surrounding area of the Reyhanlı Fault. Building on these efforts, the present study was

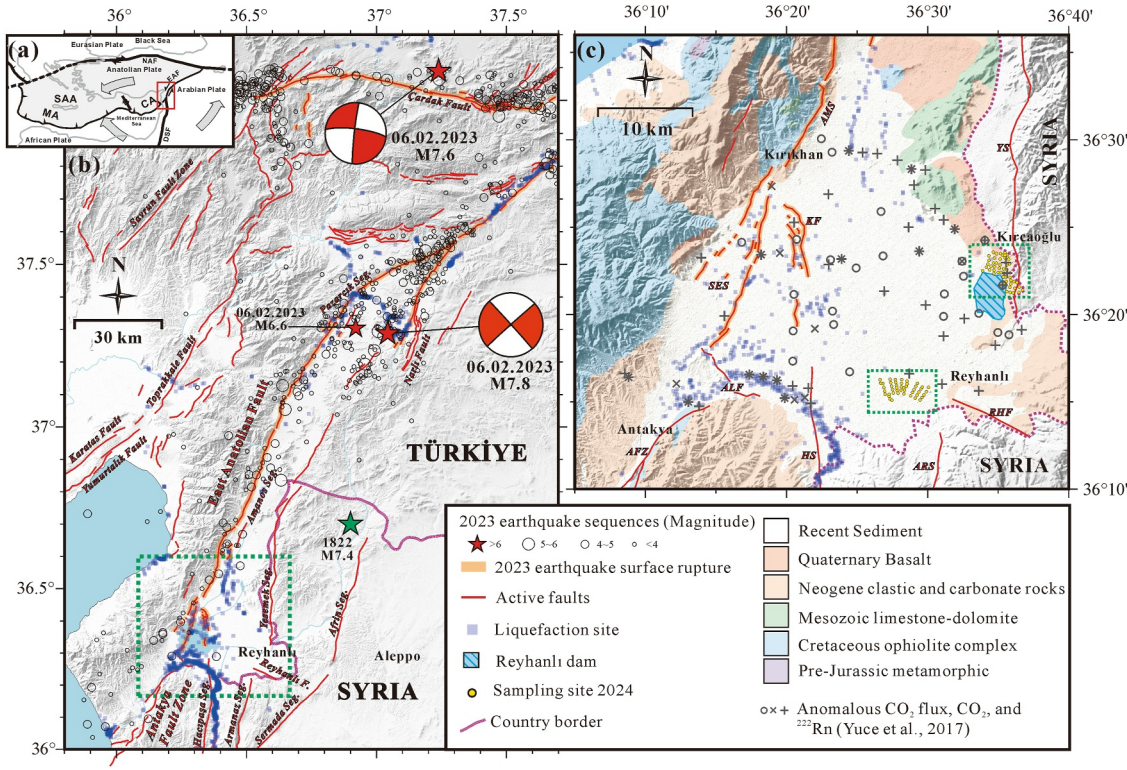

Figure 1. (a) Simplified tectonic framework of the region surrounding the study area. (b) Geological setting of southeastern Türkiye, showing the location of the study area relative to regional tectonic features. The epicenters of the 2023 Mw 7.8 and Mw 7.6 earthquakes are marked by red stars, with corresponding focal mechanisms represented by red beach ball diagrams. The blue star denotes the epicenter of the 1822 Aleppo earthquake (Ambraseys, 1989). Seismic activity recorded between 6 and 8 February 2023, is indicated by open circles. Active fault traces, compiled from Tari et al. (2013), are shown as red lines. Surface rupture zones associated with the 2023 Mw 7.8 and Mw 7.6 events are highlighted in bold orange. Blue squares indicate locations of liquefaction triggered by these earthquakes. (c) Simplified geological map of the region outlined in panel (b), showing the spatial distribution of anomalous soil gas concentrations and fluxes reported by Yuce et al. (2017). The soil gas sampling locations in the Kırcaoğlu and Reyhanlı areas are marked with yellow circles. Detailed sampling site information, including coordinates, is provided in Fu (2025).

initiated to investigate the characteristics of soil gases along potentially active, buried faults, particularly in the Kırcaoğlu and Reyhanlı regions of Hatay Province. The objectives of this study are to (a) characterize soil gas fluxes and compositions, (b) identify concealed fault traces, and (c) assess zones at elevated risk of future surface rupture.

2. Geological Background

The Hatay region in southeastern Türkiye is situated at an active plate boundary between the African, and Arabian plates (Mahmoud et al., 2005). This tectonic setting is characterized by the connection between the Dead Sea Fault (DSF) and the EAF, which are linked through the Karasu Fault (KF) or Amanos Fault (AF) in the north of the Amik basin. These major left-lateral strike-slip faults exert a dominant control on the tectonic evolution and seismic activity of the region, and are among the primary structures accommodating the westward extrusion of the Anatolian plate (Freund et al., 1968; Hempton, 1987; Saroglu et al., 1992; Sengör & Yilmaz, 1981). From a geologic perspective, the region can be broadly divided into paleotectonic and neotectonic periods. The paleotectonic period spans from the Late Cretaceous to the Miocene and is associated with the closure of the southward-subducting Tethys Ocean (Sengör & Yilmaz, 1981). The stratigraphic units of this period include extensively exposed Cretaceous ophiolites, consisting of ultramafic tectonites, gabbros, sheeted dike complexes, plagiogranites, and pillow basalts, along with deep marine sedimentary rocks such as bedded cherts and pelagic limestones that reflect the former deep oceanic environment (Dilek & Thy, 2009). Overlying these are the Campanian to Miocene-aged units, composed predominantly of carbonates and clastic sediments. The neotectonic period, beginning in the Late Miocene and continuing to the present, is closely associated with the propagation of the DSF and its linkage to the EAF. During this time, significant subsidence and sediment accumulation occurred in structural depressions such as the Amik, Karasu, and Antakya basins. These

depressions contain thick sequences of Late Cenozoic to Quaternary fluvial and volcaniclastic deposits (Boulton et al., 2006; Seyrek et al., 2007). The Quaternary alkaline basaltic volcanism has been identified along the Karasu Rift Valley, interbedded with basin-fill sediments and is interpreted as a result of neotectonic faulting and associated mantle processes (Capan et al., 1987; Rojay et al., 2001).

The Karasu Rift Valley itself is interpreted as a transtensional structure that may be classified as either a pull-apart basin or a graben formed in a left-lateral strike-slip regime (Karabacak & Altunel, 2013; Karabacak et al., 2010; Rojay et al., 2001). Based on the fault kinematic analyses, tectonic evolution reflects a transition from transpressional to transtensional deformation (Rojay et al., 2001; Över, Özden, & Yılmaz, 2004), accompanied by clockwise rotation of block-bounding faults (Tatar et al., 2004). Seismic and GPS observations support the existence of a left-lateral strike-slip fault system with extensional components (Kiratzi, 1993; McClusky et al., 2000; Reilinger et al., 1997). The Amik basin is a structurally controlled sedimentary depression located within this tectonic regime. The eastern margin of the basin corresponds to the Reyhanlı region, which is structurally influenced by the YS and RF. The YS defines the eastern boundary of the Karasu Valley, while the AF lies along its western edge (Karabulut et al., 2023). The YS is a significant left-lateral strike-slip structure. Seismic activity observed along this fault suggests that it partially accommodates relative plate motion during interseismic periods through transtensional deformation (Karabulut et al., 2023). Although active during the interseismic period, the YS displayed relatively low aftershock activity following the 2023 earthquake sequence, which may indicate a continued accumulation of tectonic stress. The RF (Emre et al., 2018; Saroglu et al., 1992) plays an important role in the structural framework of the Amik basin. This fault was developed as a right lateral strike slip transform fault between the EAF and DSF (Emre et al., 2018). Regional geological and GPS data indicate a left-lateral kinematic behavior similar to that of the YS. Together, they constitute a coupled strike-slip fault system that governs the basin's transtensional deformation and subsidence (Mahmoud et al., 2005; Rojay et al., 2001). In addition, the SSF, which represents one of the braided faults along the DSF, extends in a north-northeast to south-southwest direction from the northeastern margin of the Ghab pull-apart basin. This fault is situated west of Aleppo and has been confirmed to be active based on geomorphic evidence of left-lateral displacement and surface deformation (Karakhanian et al., 2008). North of Afrin, the Afrin Fault merges with the SSF. The SSF is considered the most probable causative fault of the destructive 1822 Aleppo earthquake (Darawcheh et al., 2022). The geological setting of the Saint Simeon Fault (SSF) is particularly relevant to this investigation because its active and braided structure, situated within the broader DSF system, contributes to a highly fractured crustal environment that promotes the migration of deep fluids and gases. The SSF has been associated with significant seismic activity, including its likely involvement in the 1822 Aleppo earthquake (Darawcheh et al., 2022), and is structurally linked to the Afrin Fault. These features enhance subsurface permeability and establish the region as a critical zone for fault-controlled degassing. A thorough understanding of this tectonic framework is therefore essential for interpreting the observed gas anomalies and fluid signatures.

The EAF and DSF represent two of the most seismically active left-lateral strike-slip fault systems along the eastern Mediterranean plate boundaries. These fault systems intersect in southeastern Türkiye near the Amik Basin, forming a tectonic triple junction (Yürür & Chorowicz, 1998; Över & Ünlügenç, 1998; Över, Kavak, et al., 2004). Since the 19th century, multiple Mw > 6.5 earthquakes have occurred along the EAF, and several prominent seismic gaps have been identified. These gaps, having experienced progressive stress accumulation, pose elevated seismic hazards. Consequently, the seismic risk along the northern DSF system is considered significant and warrants enhanced monitoring and mitigation efforts (Barbot et al., 2023; Chen et al., 2024).

Darawcheh et al. (2022) revisited the 1822 Aleppo earthquake, a catastrophic event that caused extensive destruction in southeastern Türkiye and northwestern Syria. The study identified the Saint Simeon Fault (SSF), a left-lateral strike-slip fault west of Aleppo, as the most probable source of the earthquake. Although the SSF has received limited attention in previous studies, and recent research has primarily focused on the main segments of the EAF, historical earthquake records suggest that fault systems located east of the EAF may have already accumulated significant strain energy and could interact with adjacent structures, such as the Reyhanlı Fault (RF) and Yesemek Segment (YS), particularly given the absence of major earthquakes in this area for an extended period. In addition, based on active fault mapping and integration of current seismological and paleoseismological data sets, the YS has been proposed as the most plausible rupture source for the 1822 earthquake (Duman & Emre, 2013). Other studies, however, have suggested that the event may have originated from the rupture of one of several north-south striking faults between the northern Ghab Basin and the Amik Basin (Ambraseys, 1989). It has been demonstrated that fault activity can be influenced by stress loading from past seismic events

(Freed, 2005; Freed & Lin, 2002; Sieh et al., 1989); for instance, the rupture of the Pazarcık segment of the EAF during the 2023 Mw 7.8 earthquake may have been facilitated by stress transferred from earlier historical earthquakes that occurred prior to 2019 (Sunbul, 2019). The RF, YF, and SSF are located within the southeastern extension zone of the 2023 rupture area, which itself has not experienced large-magnitude earthquakes for a long time. This spatial gap in seismicity may indicate a potential seismic gap, thereby further increasing the regional seismic hazard.

Given these considerations, in addition to continued surveillance of the EAF's main segments, it is imperative to strengthen investigations and real-time monitoring of faults along the eastern margin of the Amik Basin, particularly those adjacent to the Reyhanlı District and critical infrastructure such as the Reyhanlı Dam.

3. Methodology

In September 2024, a 7-day soil gas survey was conducted in the Kırcaoğlu and Reyhanlı regions of southeastern Türkiye to investigate spatial variations in soil gas emissions. To minimize the influence of short-term meteorological effects on the measurements (e.g., Fu et al., 2005; Yuce et al., 2017), all sampling and measurements were conducted under comparable environmental conditions characterized by overcast and rain-free weather, limited temperature variability, and negligible barometric differences across the area. These stable conditions ensured that the observed soil gas patterns primarily reflect subsurface geological controls rather than atmospheric fluctuations. A systematic, grid-based sampling approach was adopted, with inter-site spacing ranging from 100 to 500 m, depending on local accessibility and terrain.

A total of 98 sampling sites were established, comprising 52 locations in Kırcaoğlu and 46 in Reyhanlı. At each sampling point, in situ measurements of soil CO_2 flux, CO_2 concentration, and radon (^{222}Rn) concentration were conducted. In addition, gas samples were collected from selected sites exhibiting elevated flux values or anomalous gas concentrations for subsequent laboratory-based isotopic analyses. The spatial distribution of all sampling locations is illustrated in Figure 1.

3.1. CO_2 Flux Measurement

Soil CO_2 fluxes were quantified using a closed-chamber technique, following the methodology outlined in Chiodini et al. (1998), with a systematic uncertainty estimated at approximately 10%. The system comprised a custom-designed, airtight acrylic chamber (base area: 314 cm^2, height: 10 cm, and total internal volume: 3.14×10^3 cm^3) coupled with an LI-850 CO_2/H_2O gas analyzer (LI-COR Inc.), which operates within a detection range of 0–20,000 ppm and a precision of ±1.5%. A dust filter was installed at the chamber inlet to minimize particulate contamination. To ensure homogeneous mixing of the internal atmosphere, the chamber was equipped with a single inlet at the top connected to the analyzer and four lateral outlets for gas return, forming a closed-circulation loop. This configuration facilitated continuous circulation of the gas phase between the chamber and the analyzer, thereby reducing the influence of ambient air and enhancing measurement reliability. At each sampling location, the chamber was carefully placed on the soil surface to maintain an airtight seal. Soil temperature at a depth of 10 cm was recorded using a digital thermometer (ST-9215C, ATM Limited), while daily atmospheric pressure data were retrieved from the Turkish State Meteorological Service (https://www.csb.gov.tr/). These parameters were used to convert the observed rate of CO_2 concentration change (ppm/s) into flux values ($g/m^2/day$) using the following equation:

$$F_{CO_2} = k \frac{P}{S} \frac{V}{T} \frac{dc}{dt} \quad (1)$$

where F_{CO_2} is the soil CO_2 flux ($g/m^2/day$), k is the gas constant, P is atmospheric pressure (Pa), V is the chamber volume (m^3), S is the base area of the chamber (m^2), T is soil temperature (K), and dc/dt is the rate of CO_2 concentration change over time.

3.2. Soil Gas Sampling and Analytical Procedures

Soil gas sampling was conducted to determine the concentrations and isotopic compositions of gases, including CO_2, ^{222}Rn, and helium. Samples were obtained using a stainless steel probe (length: ~130 cm; diameter: 3 cm) equipped with a sharpened tip to facilitate penetration and minimize clogging. The probe was inserted into a depth

of approximately 1 m. A solid rod was then used to dislodge the tip, allowing gas to flow freely into the probe. Subsequently, the probe was connected to a custom-built gas extraction system. The system was purged for ~30 s using a hand pump to remove residual air and potential contamination from previous samples. For the determination of CO_2 concentrations, the probe was directly connected to a CO_2 analyzer. Two types of instruments were employed: a LI-850 CO_2/H_2O gas analyzer and a Guardian NG DC CO_2 detector (Edinburgh Instruments Ltd.; range: 0%–30%; precision: ±2%), collectively covering a concentration range of 1 ppm–30%. Soil gas was collected into two types of containers: (a) 3-L Tedlar bags for ^{222}Rn analysis, and (b) glass bottles for helium and carbon isotopic measurements. The glass bottles, made of potassium glass, effectively prevent helium loss by minimizing diffusive escape. Prior to fieldwork, each bottle was evacuated to create a vacuum, allowing soil gas samples to be collected and securely preserved (e.g., Fu et al., 2005; Yang et al., 2005; Yuce et al., 2017).

The concentrations of ^{222}Rn were determined using an RTM 2100 detector (SARAD GmbH), which has a measurement uncertainty of ±10%. Each analysis was conducted using a closed-circuit configuration between the sample bag and the radon detector, maintained for 30–60 min until the ^{222}Rn concentration stabilized. All samples were analyzed within several hours of collection to minimize decay-related bias (Fu et al., 2008; Walia et al., 2005; Yuce et al., 2017). Given the radioactive decay of ^{222}Rn (half-life = 3.82 days), all measured concentrations were decay-corrected using the following equation (Sensintaffar & Windham, 1990):

$$Rn_m = Rn_{initial}\, e^{-\lambda(t1-t0)} \quad (2)$$

where Rn_m is the measured ^{222}Rn concentration, $Rn_{initial}$ is the concentration at the time of sampling, λ is the decay constant (0.1813 d^{-1}), t_0 is the sampling time, and t_1 is the time of measurement.

3.3. Isotope Analysis

The helium isotopic ratios and neon concentrations were analyzed using a high-vacuum noble gas mass spectrometer (Helix, Thermo Scientific) in conjunction with a quadrupole mass spectrometer (QMS200, Pfeiffer Vacuum) at the Department of Geosciences, National Taiwan University, following analytical procedures similar to those described by Yang et al. (2005) and Lin et al. (2023). Calibration of the helium isotopic ratios was performed using both an atmospheric helium standard (Mishima et al., 2018) and a reference standard provided by the University of Tokyo, characterized by a $^3He/^4He$ ratio of 20.4 Ra, where Ra denotes the atmospheric ratio (Sano et al., 2008). The overall analytical uncertainty, accounting for both instrumental precision and long-term reproducibility, was controlled within 2% (Lin et al., 2023). Carbon isotopic compositions of soil CO_2 were measured using a Thermo Scientific MAT 253 isotope ratio mass spectrometer (IRMS) at the Institute of Oceanography, National Taiwan University, following the same analytical procedures described by Chang et al. (2012). Results were reported in $\delta^{13}C$ notation relative to the Vienna Pee Dee Belemnite (V-PDB) standard, with an analytical precision of ±0.2‰.

3.4. Graphical Statistical Analysis

To interpret the spatial variability and source contributions of emitted CO_2, graphical statistical analysis (GSA) was performed following Chiodini et al. (1998). Log-transformed CO_2 flux values were plotted on cumulative probability graphs to identify inflection points indicative of distinct populations. Based on these classifications, distribution maps of CO_2 flux were constructed to visualize emission patterns across the study area.

4. Results and Discussion

Soil gas parameters across the Kırcaoğlu and Reyhanlı regions exhibited a broad range of values, reflecting substantial spatial heterogeneity. Notably, both CO_2 and ^{222}Rn concentrations at most sampling sites were significantly elevated relative to typical atmospheric levels. For reference, ambient CO_2 concentrations are approximately 422 ppm (https://www.co2.earth), while background ^{222}Rn levels rarely exceed 100 Bq/m^3. These elevated values strongly suggest minimal dilution by atmospheric air, thereby affirming the integrity of the soil gas measurements and the predominance of subsurface gas sources. In the Kırcaoğlu area, observed CO_2 fluxes ranged from 0.1 to 18.6 $g/m^2/day$, CO_2 concentrations from 117 to 25,200 ppm, ^{222}Rn concentrations from 869 to 69,025 Bq/m^3, and soil temperatures from 25.9 to 35.0°C. In contrast, the Reyhanlı area exhibited slightly higher flux and CO_2 values, with fluxes ranging from 0.4 to 26.3 $g/m^2/day$, CO_2 concentrations from 510 to 33,000 ppm,

Table 1
Main Statistical Parameters of Soil CO_2 Flux and Gas Concentration in the Kırcaoğlu and Reyhanlı Area

Location	Type	N	Mean	Median	SD[a]	LQ[a]	UQ[a]	IQR[a]	Min	Max
Kırcaoğlu	CO_2 flux ($g/m^2/d$)	52	6.8	6.4	4.1	3.6	8.6	5.0	0.1	18.6
	CO_2 (ppm)	52	6,607	6,050	5,076	2,735	9,550	6,815	117	25,200
	Rn (Bq/m^3)	41	13,848	9,019	14,745	2,816	17,607	14,791	869	67,845
Reyhanlı	CO_2 flux ($g/m^2/d$)	46	6.3	5.1	5.3	2.6	8.8	6.2	0.4	26.3
	CO_2 (ppm)	46	7,038	4,050	7,340	2,200	10,100	7,900	510	33,000
	Rn (Bq/m^3)	46	10,029	8,656	7,716	4,666	13,180	8,514	962	40,291

[a]SD: Standard deviation; LQ: Lower quartile; UQ: Upper quartile; IQR: Interquartile rang.

^{222}Rn concentrations from 962 to 40,291 Bq/m^3, and soil temperatures spanning 23.6–36.0°C. These measurements highlight both localized degassing anomalies and broader regional patterns of soil gas emissions.

Summary statistics for soil CO_2 fluxes, gas concentrations, and soil temperature measurements from both regions are provided in Table 1, and the distributional characteristics of these variables are further visualized using box plots in Figure 2. Additionally, detailed measurements for each sampling point in the Kırcaoğlu and Reyhanlı areas are compiled in Fu (2025).

4.1. Classification of Soil CO_2 Flux and Identification of Anomalous Gas Emissions

Soil CO_2 degassing is influenced by a range of sources, typically categorized according to depth. High CO_2 flux values are commonly attributed to deep-seated origins, such as mantle or crustal degassing, whereas low fluxes

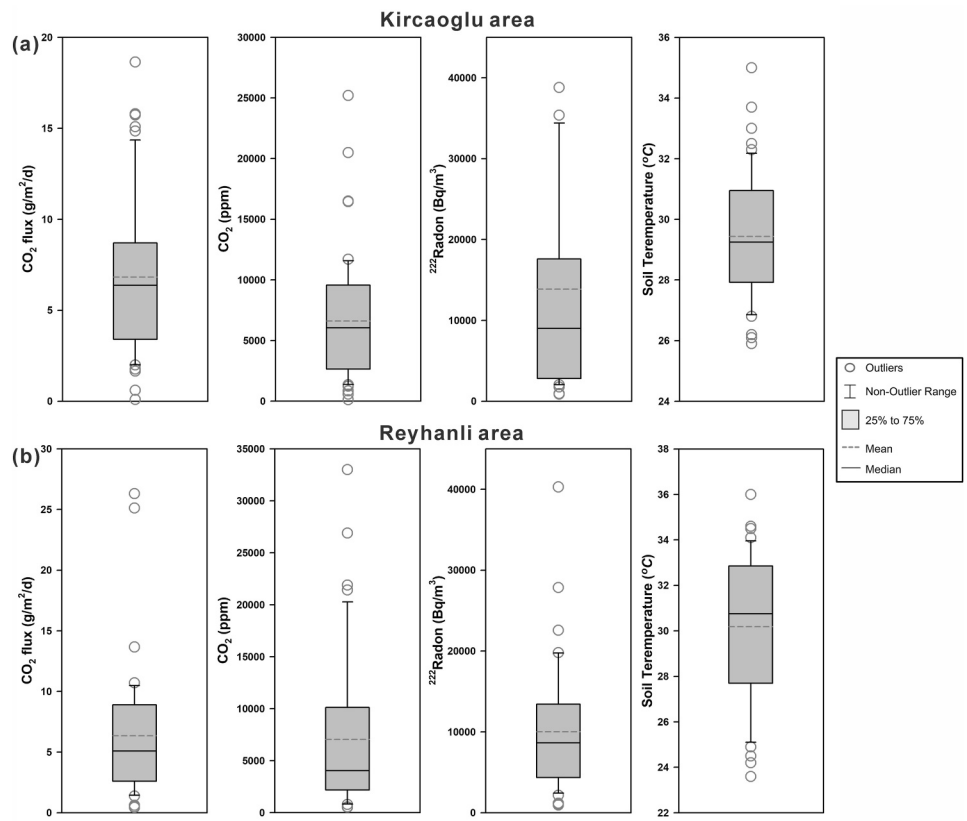

Figure 2. Box plots showing soil CO_2 flux, CO_2, and ^{222}Rn concentrations, as well as soil temperature in the (a) Kırcaoğlu and (b) Reyhanlı areas.

are primarily the result of near-surface biogenic activity. Flux values of intermediate magnitude are often interpreted as arising from a mixing of these two end-member sources (Chiodini et al., 2008). Due to this diversity in origin, soil gas flux data frequently exhibit a wide range of values and overlapping statistical distributions. To characterize and classify this variability, graphical statistical analysis (GSA) was employed. Cumulative probability plots (Sinclair, 1974) were used to identify slope changes corresponding to distinct populations within the data. These inflection points enabled the subdivision of flux data into discrete groups representing different degassing domains. This approach not only highlights anomalies within the data set but also provides insight into the underlying gas sources and their relative contributions.

In the Kırcaoğlu area, cumulative probability analysis revealed two major inflection points at approximately the 33rd (5.24 g/m^2/day) and 75th percentiles (8.54 g/m^2/day), allowing the classification of soil CO_2 fluxes into three domains (Figure 3). As summarized in Table 2, the low-domain (LD) group (Group A) accounts for 33% of the data, with a mean flux of 2.7 g/m^2/day. The medium-domain (MD) group (Group B) comprises 42% of the measurements, with a mean flux of 6.8 g/m^2/day. The high-domain (HD) group (Group C), interpreted as reflecting deep gas input, represents 25% of the samples and exhibits a mean flux of 12.3 g/m^2/day. Anomalous CO_2 fluxes in this area are thus defined by a threshold of 8.54 g/m^2/day, corresponding to the second inflection point.

Similarly, in the Reyhanlı region, inflection points on the cumulative probability curve were identified at 1.98 g/m^2/day (15th percentile) and 8.03 g/m^2/day (70th percentile). Based on these thresholds, three flux groups were also delineated (Table 2). The LD group (A) comprises 15% of the samples with a mean flux of 1.2 g/m^2/day, while the MD group (B) accounts for 55%, averaging 4.5 g/m^2/day. The HD group (C), representing 30% of the data, shows a mean flux of 12.2 g/m^2/day. The anomalous flux threshold in this area was thus set at 8.03 g/m^2/day.

In addition to CO_2 flux, cumulative probability analysis was applied to CO_2 and ^{222}Rn concentrations to identify anomalous values. In the Kırcaoğlu area, thresholds for anomalous CO_2 and ^{222}Rn concentrations were determined to be 9,500 ppm and 15,464 Bq/m^3, respectively. In contrast, the corresponding thresholds in the Reyhanlı area were 10,100 ppm for CO_2 and 11,558 Bq/m^3 for ^{222}Rn. These thresholds, derived using the same GSA method, serve to delineate zones of enhanced degassing activity.

To visualize the spatial variability of soil gas emissions, contour maps of CO_2 flux were generated using SURFER software, applying Kriging interpolation for optimal spatial estimation (Figures 4 and 5). These maps reveal the distribution and intensity of degassing anomalies, providing key insights into potential fault-related or deep-source pathways for gas migration.

4.2. The Estimation of Total CO_2 Emission

To estimate total soil CO_2 emissions within the study regions, the arithmetic mean flux value for each identified degassing domain was extrapolated over its corresponding surface area. The arithmetic mean is widely employed in such estimations due to its simplicity and its effectiveness in representing spatial variability (Chiodini et al., 1998, 2008). This method provides a first-order approximation of total CO_2 emissions and supports comparative analyses among regions and flux domains. The surveyed areas of Kırcaoğlu and Reyhanlı encompass approximately 9.7 and 9.4 km^2, respectively. Based on the surface area and the proportional distribution of flux domains as summarized in Table 2, the total soil CO_2 emissions are estimated to be 66 tonnes per day (t/d) for Kırcaoğlu and 60 t/d for Reyhanlı. Although the areas are comparable in size, the slightly higher emission rate in Kırcaoğlu may reflect relatively stronger tectonic or magmatic activity. The distribution of the three degassing domains within each area also reveals the relative contributions of background, transitional, and anomalous emissions, thereby offering insights into the underlying subsurface gas dynamics. To explore the regional-scale implications of diffuse CO_2 degassing, the same methodology was applied to the Amik Basin, which covers an estimated area of approximately 2000 km^2 (Gulen et al., 1987). According to the flux domain classification reported by Yuce et al. (2017), 24% of the basin corresponds to the low-domain (LD) group with a mean flux of 1.1 g/m^2/day, 62% to the medium-domain (MD) group with a mean flux of 6.9 g/m^2/day, and 14% to the high-domain (HD) group with a mean flux of 24.1 g/m^2/day. Based on these values, the total CO_2 emissions from the Amik Basin are estimated at approximately 15,586 t/d, as shown in Table 2. For a broader context, data from the International Energy Agency (IEA, 2024) indicate that daily energy-related CO_2 emissions in 2022 of Türkiye averaged approximately 1,068,493 t/d. Thus, diffuse soil degassing from the Amik Basin accounts for an estimated 1.5% of the country's daily CO_2 emissions, underscoring its substantial contribution despite its natural

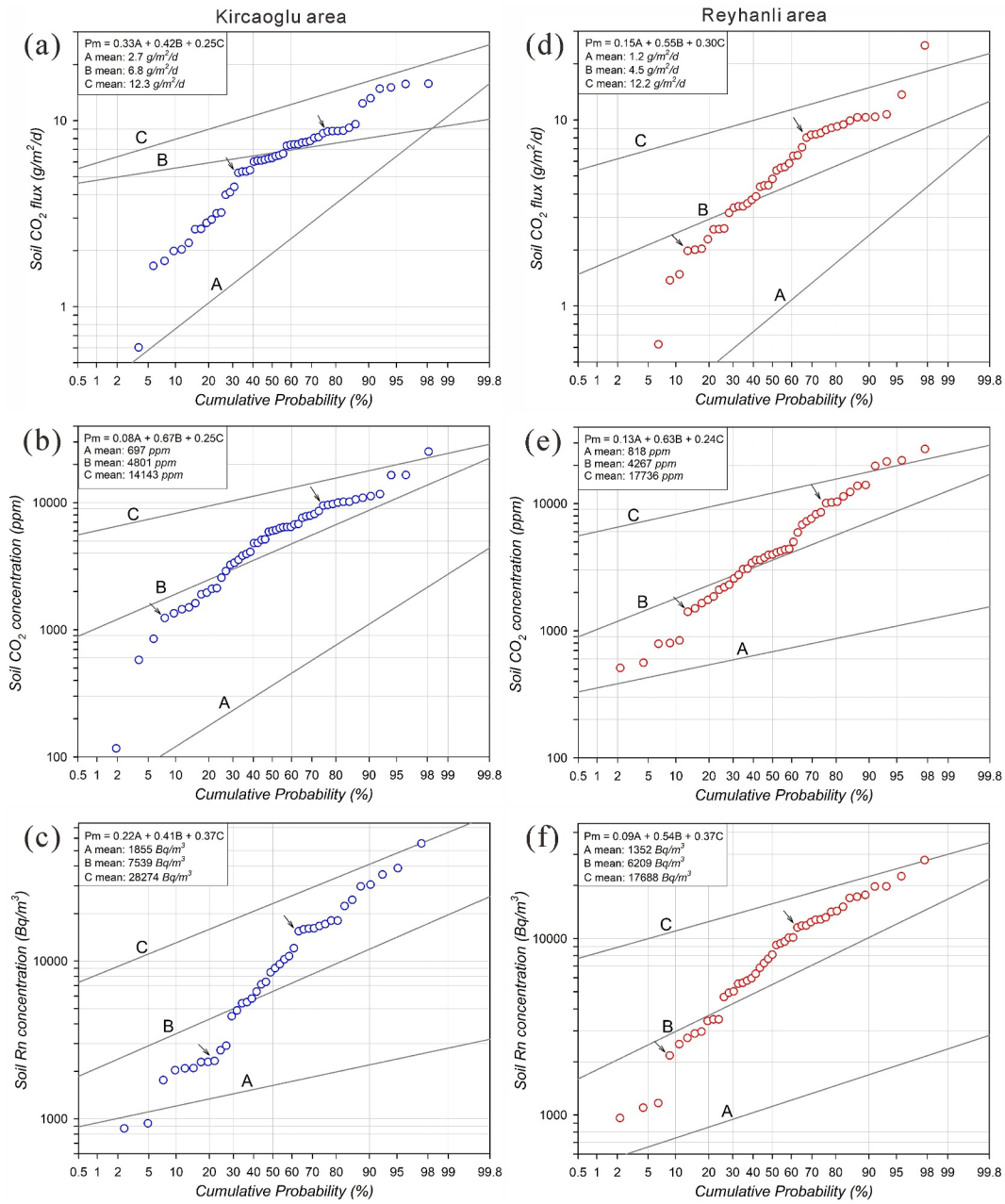

Figure 3. Cumulative probability plots of (a and d) soil CO_2 flux, (b and e) CO_2 concentration, and (c and f) ^{222}Rn concentration in the Kırcaoğlu and Reyhanlı areas, respectively. Inflection points, marked by arrows, delineate distinct populations within the data set and are used to classify the soil gas measurements into three groups: the low-domain (LD) group (A), representing background levels; the high-domain (HD) group (C), indicative of anomalous degassing; and the medium-domain (MD) group (B), representing transitional values that reflect mixed characteristics of both end-members.

origin. It is also noteworthy that the mean CO_2 fluxes recorded in Kırcaoğlu (6.8 g/m^2/day), Reyhanlı (6.3 g/m^2/day), and the Amik Basin (7.8 g/m^2/day) are relatively similar, suggesting comparable levels of tectonic and crustal activity potentially governing diffuse CO_2 emissions across these regions.

4.3. Spatial Distribution of Soil Gas Anomalies and Structural Implications

The spatial distribution of soil gas fluxes serves as an effective proxy for identifying subsurface structural features, particularly those associated with fault systems. Fault zones are typically characterized by increased

Table 2
Statistical Parameters of the Soil CO_2 Flux Populations Around the Study Area Identified From GSA

Population	Proportion	Points	Area (km^2)	Min flux ($g/m^2/d$)	Max flux ($g/m^2/d$)	Mean flux ($g/m^2/d$)	Total CO_2 output (t/d)
Kırcaoğlu							
A (LD)	33	17		0.1	5.2	2.7	8.4
B (MD)	42	22		5.3	8.5	6.8	28.0
C (HD)	25	13		8.7	18.6	12.3	29.8
Total	100	313	9.7	0.1	18.6	6.8	66.2
Reyhanlı							
A (LD)	15	7		0.4	2.0	1.2	1.7
B (MD)	55	25		2.0	8.3	4.5	23.1
C (HD)	30	14		8.4	26.3	12.2	34.8
Total	100	46	9.4	0.4	26.3	6.3	59.6
Amik basin[a]							
A (LD)	24	54		0.2	2.0	1.1	516
B (MD)	62	138		2.0	14.7	6.9	8,569
C (HD)	14	30		14.9	55.4	24.1	6501
Total	100	222	2000[b]	0.2	55.4	7.8	15,586

[a]Data from Yuce et al. (2017). [b]Data from Gulen et al. (1987).

porosity and permeability, which enhance the vertical migration of gases from deeper sources. Various gas geochemical tracers (e.g., CO_2 and ^{222}Rn) have been widely employed to delineate deformation zones, as their anomalous concentrations often coincide with both active and buried faults (Fu et al., 2005; Fu, Yang, Chen, et al., 2017; Yuce et al., 2017).

In the present investigation, spatial contour maps of CO_2 flux, CO_2 concentration, and ^{222}Rn concentration were constructed for the Kırcaoğlu area (Figures 4a–4c). To further delineate potential structurally controlled degassing zones, anomaly maps were generated based on predefined threshold values for each gas species. Regions exhibiting simultaneous anomalies in at least two gas species were classified as high soil gas anomaly zones (Figure 4d). These locations are identified as multiple anomaly sites. Their spatial clustering and preferred alignment form the principal criteria for inferring the orientations of potential structural lines or concealed faults, and adjacent multiple anomaly sites are given priority when evaluating the continuity of these features. Consistency among gas source signatures is also considered to reinforce the structural interpretation. These zones, delineated by white dashed lines, are interpreted as indicative of possible subsurface fault structures. The results reveal two prominent zones of soil gas enrichment located along the eastern and western portions of the study area. Upon closer evaluation, the eastern anomaly zone exhibits a NW–SE orientation, whereas the western anomaly zone follows a NE–SW trend and reflects a more accurate alignment with local structural and geomorphic indicators.

The eastern anomaly aligns with a NW–SE trending topographic scarp that coincides with a lithological boundary between alluvial deposits and carbonate bedrock, consistent with fault-controlled morphology. In contrast, the NE–SW oriented western anomaly spatially coincides with documented surface deformation near the Reyhanlı Dam, suggesting a buried fault that may not follow the regional structural trend. These refined orientations may reflect local structural segmentation and stress field complexities associated with the tectonic transition between the EAF and DSF systems (Rojay et al., 2001; Över, Özden, & Yılmaz, 2004). It is noteworthy that several sites exhibit anomalously high CO_2 fluxes while their CO_2 concentrations remain lower, as observed at K30, K33, and K40. This pattern suggests that in zones characterized by locally enhanced permeability or well-developed fracture networks, deep-sourced CO_2 may migrate through the overlying sediments at a relatively high flux. However, the loose, fractured, and aerated near-surface layers promote intense mixing with atmospheric air, leading to dilution of CO_2 concentrations (e.g., Fu et al., 2005). Consequently, both CO_2 and Rn concentrations near the ground surface may appear subdued. The coexistence of high flux anomalies with low gas concentrations

10.1029/2025GC012419

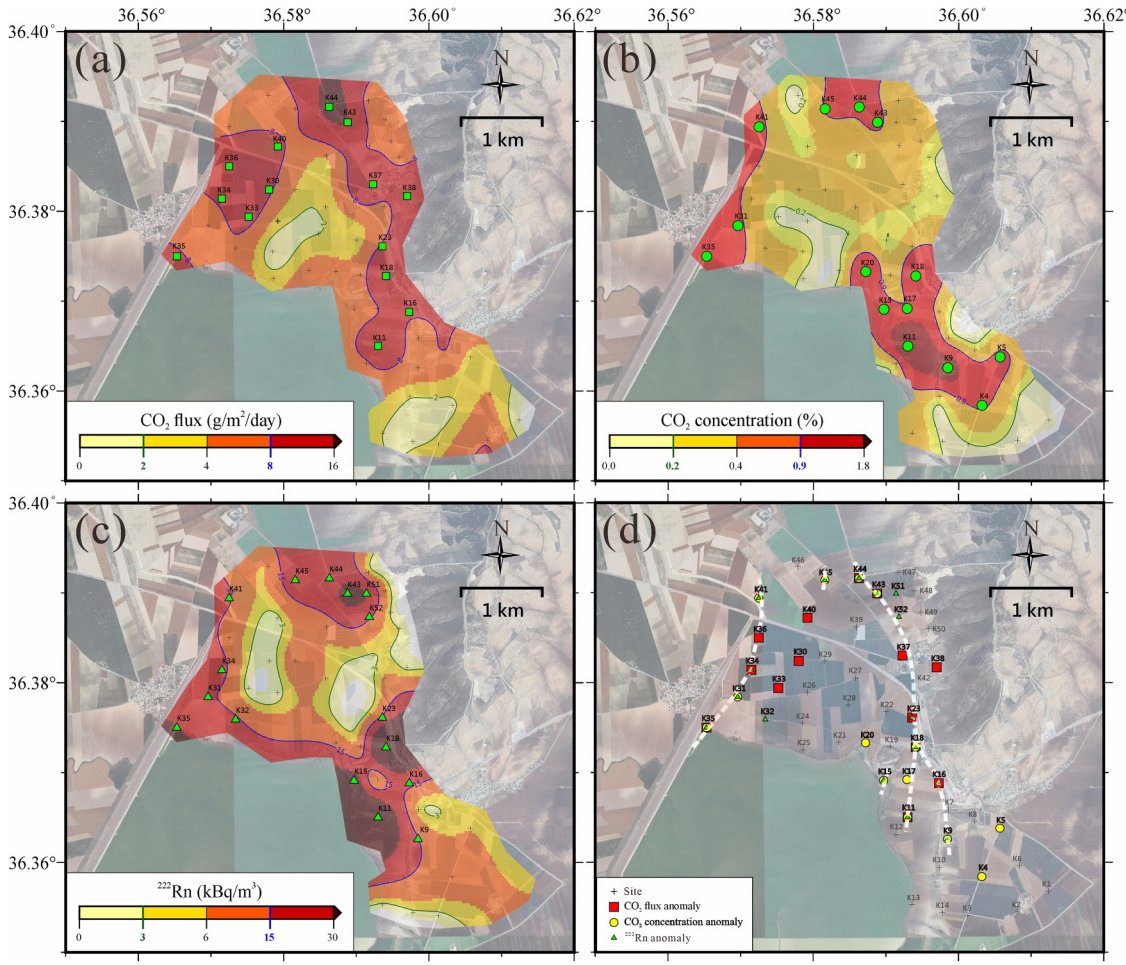

Figure 4. Spatial distribution of measured gas emissions. (a) Soil CO_2 flux, (b) CO_2 concentration, and (c) ^{222}Rn concentration in the Kırcaoğlu area. Anomalous values of soil CO_2 flux, CO_2 concentration, and ^{222}Rn concentration exceeding the threshold values of 8.54 g/m^2/day, 9,500 ppm, and 15,464 Bq/m^3, respectively, are indicated by squares, circles, and triangles. (d) Composite anomaly map showing sites with at least two overlapping gas anomalies. White dashed lines outline high-anomaly zones, interpreted as potential degassing corridors linked to buried fault structures. Crosses denote all measurement points.

is therefore not contradictory. Rather, it may reflect the presence of a concealed fault that facilitates the vertical ascent of deep gases across the western side of the Kırcaoğlu area. In this scenario, the fault zone serves as a tectonic bypass conduit that enables efficient upward gas transport, while near-surface mixing processes suppress the detectable concentration. This interpretation is consistent with the structural inference of a buried fault in this sector of the study area.

Topographically, the western portion of the Kırcaoğlu area is relatively flat and lacks any visible fault scarps or bedrock exposures. Therefore, the gas anomalies detected in this area represent the first indication of a potential buried fault beneath this region. This interpretation is further supported by the field observations reported by Çetin et al. (2025), who documented evidence of surface deformation near the Reyhanlı Dam, including prominent fractures up to 30 cm in width and vertical displacements of approximately 120 cm. These deformation features are spatially proximal to sampling sites K31 and K35, where elevated soil gas anomalies were also observed. The NE-SW orientation of this western gas anomaly is consistent with the trend of these coseismic fractures, suggesting a structurally controlled deep gas conduit beneath the dam embankment.

In the eastern part of the area, the NW-SE trending anomaly is aligned with a linear topographic scarp and a lithological contact with carbonate bedrock. The spatial coincidence between the gas anomaly, the geomorphic break, and the lithological boundary strongly supports the interpretation of the eastern scarp as a fault-controlled structure. The persistence of gas anomalies at more southern locations, including site K9, implies a southward

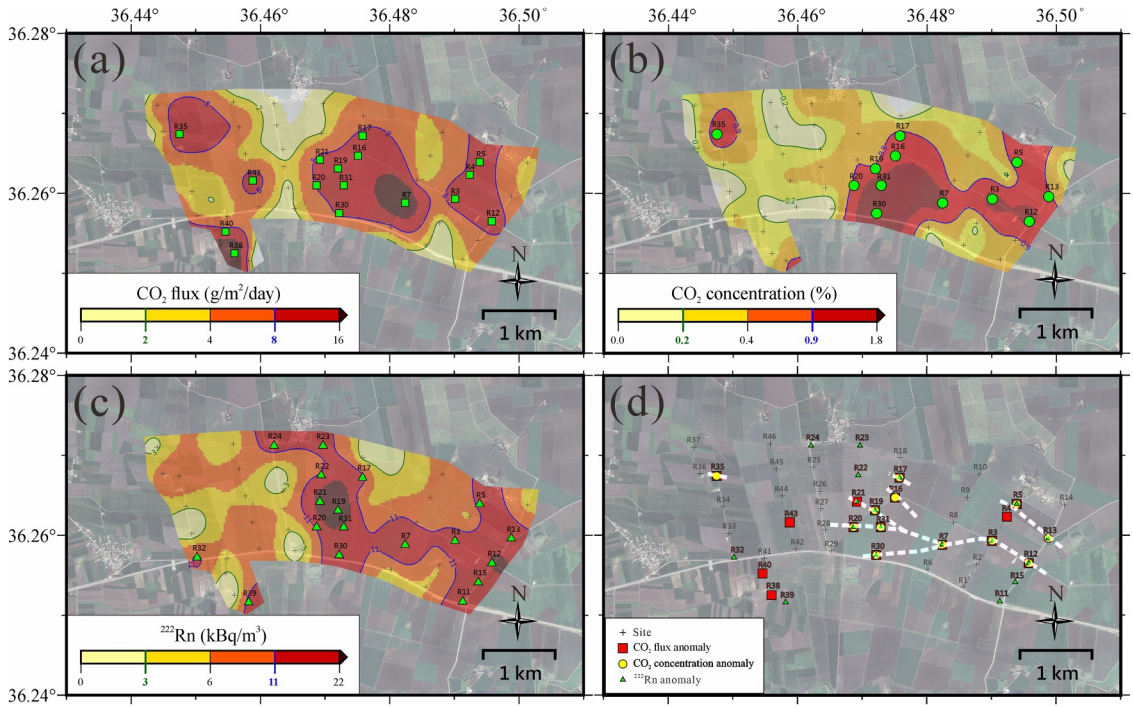

Figure 5. Spatial distribution of interpretation measured gas emissions. (a) Soil CO_2 flux, (b) CO_2 concentration, and (c) ^{222}Rn concentration in the Reyhanlı area. Anomalous values of soil CO_2 flux, CO_2 concentration, and ^{222}Rn concentration exceeding the threshold values of 8.03 g/m^2/day, 10,100 ppm, and 11,558 Bq/m^3, respectively, are indicated by squares, circles, and triangles. (d) Composite anomaly map showing sites with at least two overlapping gas anomalies. White dashed lines outline high-anomaly zones, interpreted as potential degassing corridors linked to buried fault structures. Crosses denote all measurement points.

continuation of the fault, which may present a regional seismic hazard. Notably, the eastern gas anomaly zone corresponds closely with the structural line proposed by Yuce et al. (2017), and the high-resolution gas data from this study further validate the utility of soil gas anomalies in delineating fault structures.

Additionally, radon concentrations in the eastern anomaly zone are significantly higher than those recorded in the western part of the study area (Figure 4c). This spatial contrast may be attributed to lithological differences that affect the mobility and retention of radon within the soil matrix, a phenomenon consistent with findings from previous studies (Baixeras et al., 2001; Yuce et al., 2017).

Taken together, the spatial configuration of soil gas anomalies, combined with supporting field and geological evidence, suggests the presence of two distinct subsurface fault structures in the Kırcaoğlu area. These structures may represent splays of the YS, located just north of the study region. One of these inferred faults appears to follow a NW–SE trend along the eastern topographic margin, while the other follows a NE-SW trend and continues beneath the Reyhanlı Dam. These findings highlight the utility of soil gas surveys as a non-invasive method for detecting potentially active fault systems and underscore the importance of integrating geochemical data with geological and geophysical investigations for structural interpretation and seismic risk assessment.

Figure 5 presents the spatial distribution of CO_2 flux, CO_2 concentration, and ^{222}Rn concentration in the Reyhanlı area using contour maps (Figures 5a–5c). In addition, zones of high soil gas anomalies are delineated based on threshold values for each parameter (Figure 5d). These spatial patterns provide valuable insights into potential pathways of subsurface degassing and contribute to the interpretation of underlying structural controls.

Although the topography of the Reyhanlı area is relatively subdued and no surface fault outcrops have been observed, the contour maps reveal a distinct east-west (E-W) oriented zone of elevated CO_2 flux and soil gas concentrations located in the central portion of the region. These anomalous patterns may indicate the presence of an unrecognized buried fault trending in an E-W direction. Furthermore, the spatial distribution of soil gas anomalies suggests that this potential structure may terminate within the central part of the Reyhanlı area and does not appear to extend toward the western boundary. This inferred structural feature may correspond to a previously unidentified buried fault or represent a westward extension of the Reyhanlı Fault originating from the eastern

Table 3
Chemical and Isotopic Composition of Soil Gases in the Study Area Collected From September 2024

ID	$\delta^{13}C_{CO_2}$ (‰)	$^3He/^4He$ (R/Ra)	$^4He/^{20}Ne$	^3He (ppm)	^4He (ppm)	A[a]	C (%)[a]	M[a]
K11	−21.0	1.00	0.336	7.32E−06	5.26	94.6	4.7	0.7
K18	−14.4	0.92	0.338	7.14E−06	5.59	93.8	6.2	0
K35	−15.0	0.97	0.341	7.08E−06	5.22	93.2	6.3	0.5
K37	−23.5	1.01	0.340	7.21E−06	5.13	93.4	5.7	0.9
K43	−22.7	1.00	0.346	7.29E−06	5.23	91.9	7.1	1
R7	−21.9	1.00	0.337	7.15E−06	5.16	94.5	4.9	0.6
R12	−20.1	0.98	0.319	7.19E−06	5.28	99.4	0.6	0
R16	−20.8	1.01	0.333	7.19E−06	5.10	95.4	3.9	0.7
R30	−22.3	1.02	0.337	7.19E−06	5.09	94.4	4.7	0.9
R35	−22.8	1.01	0.341	7.23E−06	5.14	93.4	5.7	0.9
A9[b]	−5.6[c]	1.04	13.5	1.90E−05	13.59	2	82	16
A10[b]	−11.3[c]	0.89	0.315	7.53E−06	5.78	84	15	1

[a]A, C, and M denote contributions from air-saturated water, the crustal component, and the mantle component, respectively, following the classification of Sano and Wakita (1985). [b]Data on dissolved gases in spring water from the Kırcaoğlu area were obtained from Yuce et al. (2014). [c]C-isotopic composition of total dissolved inorganic carbon (TDIC) was obtained from Yuce et al. (2014).

sector of the study area. If this interpretation is accurate, the total length of the Reyhanlı Fault would exceed previous estimates, which would also imply an increase in its associated seismic hazard potential.

Irrespective of its precise geological origin, the structural anomaly identified in this study, whether a newly recognized feature or an extension of the RF, is reported here for the first time. Its identification emphasizes the importance of high-resolution soil gas surveys for fault detection and highlights the necessity for continued geophysical and geological investigations to evaluate its potential tectonic significance.

4.4. Sources of the Soil Gases

To investigate the origins of soil gases, this study combined multiple geochemical approaches. In addition to analyzing the correlation between CO_2 and ^{222}Rn, 10 representative soil gas samples were selected from the Kırcaoğlu and Reyhanlı regions based on elevated CO_2 fluxes or anomalously high gas concentrations. Five samples were collected from each area for helium and carbon isotopic analyses (Table 3), providing further constraints on gas source characteristics.

Helium isotopes serve as robust tracers for distinguishing between atmospheric, crustal, and mantle-derived components. To quantify the contribution of each, the three-component mixing model developed by Sano and Wakita (1985) was applied. The assumed end-member values are as follows: for air, the ($^4He/^{20}Ne$) and ($^3He/^4He$) ratios are 0.318 and 1 Ra, respectively (Sano et al., 1982); for crustal and mantle sources, the ($^4He/^{20}Ne$) ratios are both set at 1000, while the ($^3He/^4He$) values are 0.02 Ra and 8 Ra, respectively (Sano & Wakita, 1985). As summarized in Table 3 and shown in Figure 6a, soil gas samples from Kırcaoğlu and Reyhanlı exhibit $^3He/^4He$ ratios ranging from 0.92 to 1.01 Ra and 0.98 to 1.02 Ra, respectively. The corresponding $^4He/^{20}Ne$ ratios range from 0.319 to 0.346, exceeding atmospheric or air-saturated water (ASW) benchmarks of 0.265 and 0.318 (O'Nions & Oxburgh, 1988; Smith & Kennedy, 1983). These results suggest measurable contributions from crustal helium, with maximum estimated proportions of 7.1% in Kırcaoğlu and 5.7% in Reyhanlı. In contrast, mantle-derived helium is minimal, contributing less than 1% in both areas. Ternary mixing analysis indicates that soil gas compositions in both regions are dominated by crustal and atmospheric sources. This pattern is consistent with previous observations of soil gas from fault zones in the Amik Basin, though it differs from the isotopic signatures observed in dissolved gas samples from the same region (Yuce et al., 2014, 2017). For comparison, helium isotope analyses of spring and cold spring samples from the Kırcaoğlu area yielded values of 1.04 Ra and 0.89 Ra for samples A9 and A10, respectively. The estimated contributions of mantle helium were 16% and 1%, while crustal contributions were 82% and 15% (Yuce et al., 2014). These spring gases,

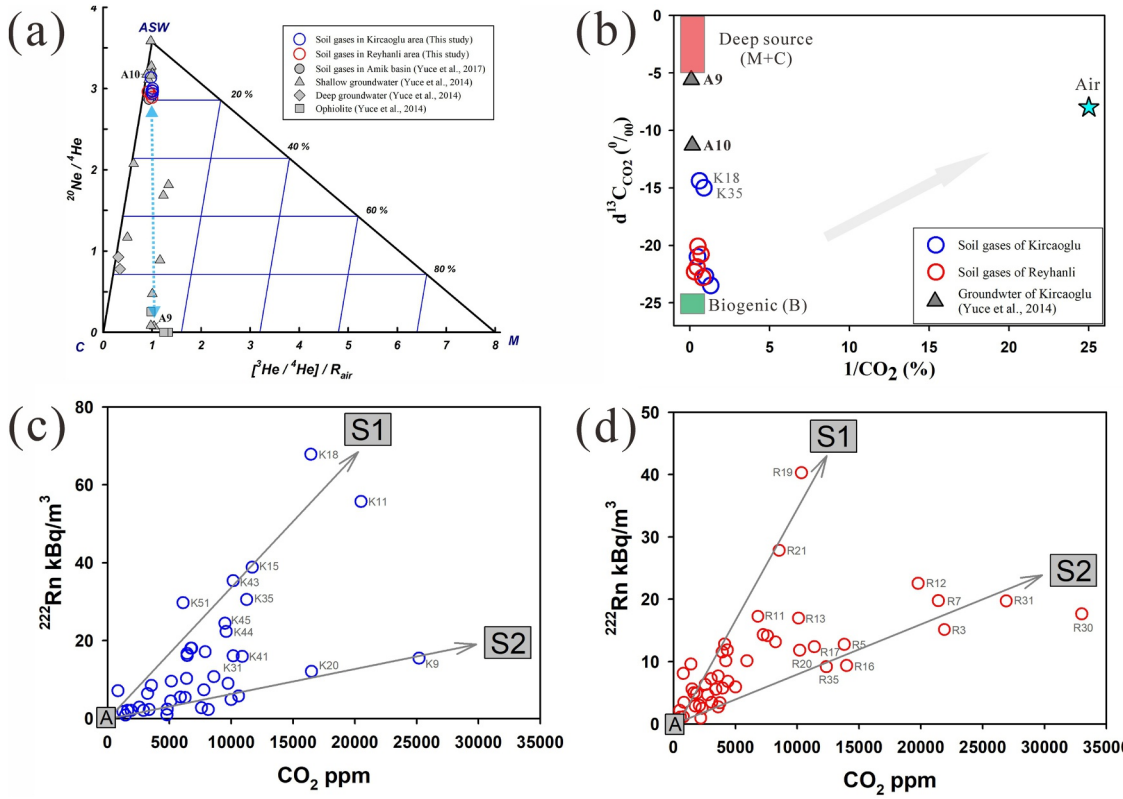

Figure 6. (a) Plot showing variations in CO_2 and ^{222}Rn concentrations in the Kırcaoğlu and (b) Reyhanlı areas. Three primary endmembers are identified: (A) atmospheric source, characterized by low CO_2 and Rn concentrations, (S1) deep source, distinguished by elevated concentrations of both CO_2 and Rn, and (S2) shallow source, marked by high CO_2 but low Rn concentrations. (c) Ternary diagram of helium isotopic composition in representative soil gas samples from the Kırcaoğlu and Reyhanlı regions. Data from soil gas, groundwater, and ophiolite samples in the Amik Basin are also shown for comparison (data from Yuce et al., 2014, 2017). ASW: air-saturated water; C: crustal component; M: mantle component. (d) Plot of $\delta^{13}C_{CO2}$ versus $1/CO_2$ values from soil gas samples. The deep source (M + C) represents a mixture of mantle and crustal endmembers (Sano & Marty, 1995), the biogenic source (B) corresponds to biogenic input (Hoefs, 2009), and the air source reflects the atmospheric endmember.

collected from bubbling pools connected to deep hydrothermal conduits, are interpreted as minimally affected by shallow contamination. In contrast, soil gas samples collected at a depth of approximately 1 m are more likely to be influenced by air mixing or shallow biological activity, which dilutes the signal of deep-sourced gases during their ascent. To estimate the extent of dilution, a simplified two-endmember mixing calculation was conducted using spring sample A9 as the deep endmember and soil sample K43 as the air-diluted endmember. The results suggest that mantle and crustal helium in the soil gas sample constitute only 8.7% and 6.3%, respectively, of their original proportions. This implies that deep helium signals are substantially attenuated during upward migration through fault systems, with only about 7% of the original signal remaining in near-surface soil gases.

As shown in Figure 6b, $\delta^{13}C_{CO_2}$ values in soil gas from the Kırcaoğlu area range from −23.5‰ to −14.4‰, while those in Reyhanlı range from −22.8‰ to −20.1‰. These values fall between the characteristic deep endmembers and biogenic endmembers, consistent with a mixing origin. Based on typical $\delta^{13}C_{CO_2}$ signatures, mantle- and crust-derived CO_2 exhibit values of approximately −6.5 and 0‰, respectively, while atmospheric and biogenic endmembers are around −7 and −25‰ (Hoefs, 2009; Sano & Marty, 1995). Most samples plot between the deep endmember (M + C) and the biogenic endmember (B), with slight atmospheric influence observed in some cases. The $\delta^{13}C$ distribution in Kırcaoğlu indicates a more prominent contribution from deep-sourced CO_2, which is consistent with the helium isotope results and suggests enhanced vertical gas migration through fault structures. In Reyhanlı, $\delta^{13}C_{CO_2}$ values suggest greater influence from biogenic sources, likely resulting from aerobic microbial respiration in the soil (F. L. Liu et al., 2023). This biogenic dominance also explains the relatively low contributions of both crustal and mantle helium in Reyhanlı compared to Kırcaoğlu.

Radon and CO_2 are widely recognized as effective geochemical tracers for identifying subsurface gas sources and transport mechanisms. The utility of radon stems from its extremely low diffusion coefficient in porous media, which restricts its ability to migrate over long distances under normal geological conditions. In the absence of nearby radon-generating lithologies, such as uranium-rich rocks, the detection of radon at the surface is generally interpreted as the result of advective transport. This process is typically facilitated by accompanying gases, known as carrier gases, that enable the upward migration of radon from depth (e.g., Fu et al., 2005; Yang et al., 2003). As shown in Figures 6c and 6d, the CO_2 and ^{222}Rn data from the Kırcaoğlu and Reyhanlı regions reveal two distinct endmembers beyond the atmospheric component (A), designated as S1 and S2. The S1 endmember is characterized by simultaneous enrichment in both CO_2 and radon, suggesting a deeper-seated gas source with limited shallow interference. In contrast, the S2 endmember displays elevated CO_2 concentrations but only modest radon enrichment, implying a relatively shallower deep source or a different migration pathway. The distinct slopes observed in the CO_2-radon correlation between these two groups support the existence of at least two gas endmembers originating from different depths or structural domains. This interpretation is further corroborated by the carbon isotopic results (Figure 6b), which show that S1-type samples exhibit relatively heavier $\delta^{13}C$ values, consistent with a stronger contribution from deep-sourced CO_2. In contrast, the more depleted $\delta^{13}C$ values observed in S2-type samples may reflect partial overprinting by near-surface processes such as microbial respiration or organic carbon oxidation during upward migration. Taken together, these geochemical patterns indicate that both S1 and S2 are linked to deep gas origins but likely represent distinct degassing pathways or structural domains with different degrees of interaction with the shallow environment.

4.5. Integrated Interpretation of Gas Origins and Structural Controls

To synthesize the geochemical, isotopic, and structural evidence obtained in this study, we provide an integrated interpretation of gas origins and their spatial relationships with subsurface fault architecture in the Kırcaoğlu-Reyhanlı region. Our multi-parameter analysis reveals a complex degassing system in which both shallow and deep sources contribute to the observed soil gas anomalies, with fault-related structures acting as preferential pathways that control the vertical migration and surface expression of these gases.

To further illustrate the complexity of $\delta^{13}C$ interpretation, we examine sample K11, which presents an apparent inconsistency between its geochemical and isotopic signatures. Although classified as part of the S1 group, K11 shows a $\delta^{13}C$ value of approximately $-21‰$, which falls within the typical range of biogenic CO_2. At this site, elevated CO_2 flux, high CO_2 concentration, and strong ^{222}Rn anomalies were observed, collectively suggesting a structurally fractured and highly permeable zone that facilitates efficient gas migration. However, the $\delta^{13}C$ value implies that the near-surface CO_2 is predominantly influenced by shallow biogenic processes. These contrasting observations are not contradictory. Fault damage zones primarily enhance vertical transport but do not alter the original source isotopic signature. In cases where the proportion of deep-sourced CO_2 is relatively low, upward migrating gas may undergo isotopic dilution through shallow biogenic overprinting, particularly within loose, aerated sediments (e.g., Fu et al., 2005). As a result, the measured $\delta^{13}C$ may underestimate the true deep contribution. Furthermore, elevated radon values reflect structural permeability rather than the origin of CO_2 itself. The combination of high CO_2 flux and Rn concentrations, together with a biogenic-like $\delta^{13}C$ value, likely indicates a gas escape window with high permeability but limited deep CO_2 input.

To quantify these observations and assess the relative proportions of deep CO_2 input, we applied a two-endmember isotopic mixing model using $-25‰$ and $0‰$ as the representative endmembers for biogenic and crustal CO_2, respectively (Chiodini et al., 2008). The results indicate that sample K11 has a deep CO_2 proportion of only 16%, meaning that out of its total CO_2 concentration of 20,500 ppm, approximately 3,280 ppm is derived from a deep source. Among all samples with available $\delta^{13}C$ data (Table 3), K18 and K35 exhibit the most prominent deep signatures, with deep-source proportions of 42% and 40%, corresponding to roughly 6,975 ppm and 4,500 ppm of deep-derived CO_2, respectively. For the remaining samples, the average deep CO_2 contribution is approximately 10%, indicating that most of the measured CO_2 is dominated by biogenic components.

Despite these quantitative estimates, the limited spatial coverage of isotopic data constrains the broader applicability of deep CO_2 mapping across the study area. As a result, it is currently not feasible to construct a comprehensive spatial map of deep-corrected CO_2 concentrations or to directly assess their structural correlation. Nevertheless, although shallow biogenic processes may overprint $\delta^{13}C$ signatures and obscure deep-sourced CO_2

contributions, the detection of relatively heavier $\delta^{13}C$ values serves as strong geochemical evidence for a genuine deep origin.

The crustal thickness beneath the study area is approximately 10 km (Keskin, 2003), a setting consistent with widespread Neogene volcanic activity and the presence of relatively young basaltic eruptions (Rojay et al., 2001). Moreover, stratigraphic profiles from boreholes in the Reyhanlı Dam area reveal that basaltic basement is encountered at a depth of approximately 25 m (Çetin et al., 2025). This suggests that mantle-derived fluids may ascend through reactivated magmatic pathways. Torfstein et al. (2013) and Yuce et al. (2014) proposed that deep mantle-derived CO_2 can act as a carrier gas, facilitating the upward migration of volatiles through the active DSF system and eventually reaching the surface (Inguaggiato et al., 2016). Within the Amik Basin, the DSF and EAF systems play a key role in controlling the degassing of both mantle- and crustal-derived volatile components (Yuce et al., 2014, 2017). Accordingly, the YS, as part of the EAF system (Kürçer, Domaç Yalçın, et al., 2025; Kürçer, Elmacı, et al., 2025), together with the adjacent RF, as a segment of the DSF system (Duman & Emre, 2013), is expected to exert a significant influence on the release of deep-sourced gases.

Results from the present soil gas investigation indicate that both the Kırcaoğlu and Reyhanlı areas exhibit a mixture of deep and shallow gas components. Previously unrecognized linear structures were identified in both regions based on high soil gas fluxes and elevated gas concentrations. These features suggest the development of deep-seated rupture zones along buried fault branches of the DSF and EAF systems, which serve as conduits for deep gas migration toward the surface. Moreover, the gas anomalies observed in the Kırcaoğlu area are slightly more pronounced than those in the Reyhanlı area, potentially implying that the Yesemek segment may exhibit a higher degree of tectonic activity compared to the Reyhanlı Fault.

Taken together, our findings suggest that the degassing patterns observed in this study reflect the interplay of complex geochemical signatures, isotopic overprinting, and crustal-scale structural controls. The integration of multi-parameter geochemical data with geological context highlights the utility of soil gas surveys for identifying active fault zones and provides valuable insight into deep fluid transport processes in seismically active regions.

5. Conclusions

This study presents a systematic soil gas geochemical investigation conducted in the Kırcaoğlu and Reyhanlı regions of Hatay Province, Türkiye, in the context of the 2023 Kahramanmaraş earthquake sequence. The primary findings are as follows:

1. Based on the spatial distribution of soil gas anomalies, two north-south trending potential buried fault structures were identified in the Kırcaoğlu area, one of which extends beneath the Reyhanlı Dam. These findings underscore the effectiveness of soil gas investigations in delineating structurally controlled degassing zones in areas lacking visible surface fault expressions. This discovery holds significant implications for re-evaluating seismic hazard potential, particularly in densely populated areas and near critical infrastructure.
2. In the Reyhanlı region, a prominent east-west trending soil gas anomaly was identified in the central part of the study area, suggesting a possible westward extension of the RF. If confirmed, this extension would substantially increase the estimated fault length and consequently elevate the associated seismic hazard potential.
3. Isotopic analyses of CO_2 and helium in the Kırcaoğlu region reveal that while most samples are dominated by biogenic contributions, several sites exhibit relatively heavy $\delta^{13}C$ values and elevated $^3He/^4He$ ratios, indicating the presence of crustal or mixed deep-sourced gases. These isotopic fingerprints, despite possible shallow overprinting, support the interpretation of distinct degassing pathways and varying degrees of deep-shallow interaction across structurally controlled gas migration zones.
4. Natural CO_2 emissions were estimated at approximately 66 and 60 t/d for the Kırcaoğlu and Reyhanlı areas, respectively, while the broader Amik Basin was estimated to emit approximately 15,586 t/d. These considerable fluxes, in combination with spatial gas anomalies and permeability-enhanced zones, may reflect the ongoing release of tectonic stress and highlight the relevance of fluid-fault coupling processes in this complex tectonic setting.
5. Previous studies have shown a strong spatial correlation between soil gas anomalies and zones of surface rupture and liquefaction induced by the 2023 earthquakes (Taftsoglou et al., 2023; Yuce et al., 2017). Building upon this foundation, the present study identified several new zones of gas anomalies that delineate previously unrecognized fault structures and may represent areas of elevated seismic risk. These findings further validate

the application of soil gas surveys in buried fault detection and emphasize their importance in seismic hazard assessment frameworks.

Conflict of Interest

The authors declare no conflicts of interest relevant to this study.

Data Availability Statement

The database includes the site locations, CO_2 fluxes, CO_2 and radon concentrations, and soil temperatures measured in the Kırcaoğlu and Reyhanlı areas can be found at Mendeley Data from Fu (2025).

Acknowledgments
We are grateful for the assistance with isotopic analysis provided by Ms. Jui-Fen Tsai, Mr. Po-Yu Chen, and Mr. Kuo-Wei Wu. This work was funded by the Scientific and Technological Research Council of Turkey (TUBITAK), project no. 123Y301, and by the Scientific Research Projects Coordination Unit of Hacettepe University under Grant 21551. The research was also supported by Grants NSTC 112-2628-M-001-005, which is funded through the National Science and Technology Council (NSTC).

References

Ambraseys, N. N. (1989). Temporary seismic quiescence: SE Turkey. *Geophysical Journal International*, *96*(2), 311–331. https://doi.org/10.1111/j.1365-246X.1989.tb04453.x

Annunziatellis, A., Beaubien, S. E., Bigi, S., Ciotoli, G., Coltella, M., & Lombardi, S. (2008). Gas migration along fault systems and through the vadose zone in the Latera caldera (Central Italy): Implications for CO_2 geological storage. *International Journal of Greenhouse Gas Control*, *2*(3), 353–372. https://doi.org/10.1016/j.ijggc.2008.02.003

Baixeras, C., Erlandsson, B., Font, L., & Jönsson, G. (2001). Radon emanation from soil samples. *Radiation Measurements*, *34*(1–6), 441–443. https://doi.org/10.1016/S1350-4487(01)00203-7

Barbot, S., Luo, H., Wang, T., Hamiel, Y., Piatibratova, O., Muhammad, T., et al. (2023). Slip distribution of the February 6, 2023 Mw 7.8 and Mw 7.6, Kahramanmaraş, Turkey earthquake sequence in the East Anatolian Fault Zone. *Seismica*, *3*(2), 502. https://doi.org/10.26443/seismica.v2i3.502

Boulton, S., Robertson, A. H. F., & Ünlügenç, U. C. (2006). Tectonic and sedimentary evolution of the Cenozoic Hatay Graben, Southern Turkey: A two-phase model for graben formation. In A. H. F. Robertson & D. Mountrakis (Eds.), *Tectonic development of the Eastern Mediterranean Region* (Vol. 260, pp. 613–634). Geological Society special publication. https://doi.org/10.1144/GSL.SP.2006.260.01.26

Capan, U. Z., Vidal, P., & Cantagrel, J. M. (1987). K-Ar, Nd, Sr and Pb isotopic study of the Quaternary volcanism in Karasu Rift (Hatay), N-end of Dead Sea rift zone in SE Turkey. *Hacettepe Üniversitesi Yerbilimleri*, *14*, 165–178.

Caracausi, A., Camarda, M., Chiaraluce, L., De Gregorio, S., Favara, R., & Pisciotta, F. A. (2023). A novel infrastructure for the continuous monitoring of soil CO_2 emissions, a case study at the Alto Tiberina near Fault Observatory in Italy. *Frontiers of Earth Science*, *11*, 1172643. https://doi.org/10.3389/feart.2023.1172643

Carena, S., Friedrich, A. M., Verdecchia, A., Kahle, B., Rieger, S., & Kübler, S. (2023). Identification of source faults of large earthquakes in the Turkey-Syria Border Region between 1000 CE and the present, and their relevance for the 2023 Mw 7.8 Pazarcık earthquake. *Tectonics*, *42*(12), e2023TC007890. https://doi.org/10.1029/2023TC007890

Çetin, K. O., Ayhan, B. U., Cüceoğlu, F., & Sefa Yildirim, S. (2025). Performance of Reyhanlı Dam during February 6, 2023 Kahramanmaraş-Türkiye earthquake sequence. *Soil Dynamics and Earthquake Engineering*, *194*, 109369. https://doi.org/10.1016/j.soildyn.2025.109369

Chang, Y. H., Cheng, T. W., Lai, W. J., Tsai, W. Y., Sun, C. H., Lin, L. H., & Wang, P. L. (2012). Microbial methane cycling in a terrestrial mud volcano in eastern Taiwan. *Environmental Microbiology*, *14*(4), 895–908. https://doi.org/10.1111/j.1462-2920.2011.02658.x

Chen, J., Liu, C., Dal Zilio, L., Cao, J., Wang, H., Yang, G., et al. (2024). Decoding stress patterns of the 2023 Turkiye-Syria earthquake doublet. *Journal of Geophysical Research: Solid Earth*, *129*(10), e2024JB029213. https://doi.org/10.1029/2024JB029213

Chiodini, G., Caliro, S., Cardellini, C., Avino, R., Granieri, D., & Schmidt, A. (2008). Carbon isotopic composition of soil CO_2 efflux, a powerful method to discriminate different sources feeding soil CO_2 degassing in volcanic-hydrothermal areas. *Earth and Planetary Science Letters*, *274*(3–4), 372–379. https://doi.org/10.1016/j.epsl.2008.07.051

Chiodini, G., Cardellini, C., Luccio, F. D., Selva, J., Ventura, G., Caliro, S., et al. (2020). Correlation between tectonic CO_2 earth degassing and seismicity is revealed by a 10-year record in the Apennines, Italy. *Science Advances*, *6*(35), 2938. https://doi.org/10.1126/sciadv.abc2938

Chiodini, G., Cioni, R., Guidi, M., Raco, B., & Marini, L. (1998). Soil CO_2 flux measurements in volcanic and geothermal areas. *Applied Geochemistry*, *13*(5), 543–552. https://doi.org/10.1016/S0883-2927(97)00076-0

Ciotoli, G., Bigi, S., Tartarello, C., Sacco, P., Lombardi, S., Ascione, A., & Mazzoli, A. (2014). Soil gas distribution in the main coseismic surface rupture zone of the 1980, Ms = 6.9, Irpinia Earthquake (southern Italy). *Journal of Geophysical Research: Solid Earth*, *119*(3), 2440–2461. https://doi.org/10.1002/2013JB010508

Cui, Y. J., Li, Y., Zheng, W., Huang, J. N., Zeng, Z. J., Liu, Z. F., et al. (2024). CH_4 and CO_2 emissions from different tectonic settings along the western margin of the Ordos Block in China: Output and correlation with the regional tectonics. *Geochemistry, Geophysics, Geosystems*, *25*(8), e2024GC011661. https://doi.org/10.1029/2024GC011661

D'Alessandro, W., Li Vigni, L., Gagliano, A. L., Calabrese, S., Kyriakopoulos, K., & Daskalopoulou, K. (2020). CO_2 release to the atmosphere from thermal springs of Sperchios Basin and northern Euboea (Greece): The contribution of "hidden" degassing. *Applied Geochemistry*, *119*, 104660. https://doi.org/10.1016/j.apgeochem.2020.104660

Dal Zilio, L., & Ampuero, J. P. (2023). Earthquake doublet in Turkey and Syria. *Communications Earth & Environment*, *4*(1), 71. https://doi.org/10.1038/s43247-023-00747-z

Darawcheh, R., Abdul-Wahed, M. K., & Hasan, A. (2022). The Great 1822 Aleppo Earthquake: New historical sources and strong ground motion simulation. *Geofísica Internacional*, *61*(3), 201–228. https://doi.org/10.22201/igeof.00167169p.2022.61.3.2198

Dilek, Y., & Thy, P. (2009). Island arc tholeiite to boninitic melt evolution of the Cretaceous Kizildag (Turkey) ophiolite: Model for multi-stage early arc-forearc magmatism in Tethyan subduction factories. *Lithos*, *113*(1–2), 68–87. https://doi.org/10.1016/j.lithos.2009.05.044

Doğan, T., Sumino, H., Nagao, K., Notsu, K., Tuncer, M. K., & Celik, C. (2009). Adjacent releases of mantle helium and soil CO_2 from active faults: Observations from the Marmara region of the North Anatolian Fault zone, Turkey. *Geochemistry, Geophysics, Geosystems*, *10*(11), Q11009. https://doi.org/10.1029/2009GC002745

Duman, T. Y., & Emre, Ö. (2013). The East Anatolian Fault: Geometry, segmentation and jog characteristics. In A. H. F. Robertson, O. Parlak, & U. C. Ünlügenç (Eds.), *Geological development of Anatolia and the easternmost Mediterranean region* (Vol. 72, pp. 495–529). Geological Society special publication. https://doi.org/10.1144/SP372.14

Emre, Ö., Duman, T. Y., Özalp, S., Şaroğlu, F., Olgun, Ş., Elmacı, H., & Çan, T. (2018). Active fault database of Turkey. *Bulletin of Earthquake Engineering*, *16*(8), 3229–3275. https://doi.org/10.1007/s10518-016-0041-2

Erdik, M., Tümsa, M. B. D., Pinar, A., Altunel, E., & Zülfikar, A. C.(2023). A preliminary report on the February 6, 2023 earthquakes in Türkiye. *Temblor*. https://doi.org/10.32858/temblor.297

Freed, A. M. (2005). Earthquake triggering by static, dynamic, and postseismic stress transfer. *Annual Review of Earth and Planetary Sciences*, *33*(1), 335–367. https://doi.org/10.1146/annurev.earth.33.092203.122505

Freed, A. M., & Lin, J. (2002). Accelerated stress buildup on the southern San Andreas Fault and surrounding regions caused by Mojave Desert earthquakes. *Geology*, *30*(6), 571–574. https://doi.org/10.1130/0091-7613(2002)030<0571:ASBOTS>2.0.CO;2

Freund, R., Zak, I., & Garfunfel, Z. (1968). On the age and rate of sinistral movement along the Dead Sea rift. *Nature*, *220*, 253–255. https://doi.org/10.1038/220253a0

Fu, C. C. (2025). The site locations, CO_2 fluxes, CO_2 and radon concentrations, and soil temperatures measured in the Kırcaoğlu and Reyhanlı areas [Dataset]. *Mendeley Data*, *V1*. https://doi.org/10.17632/wch4pz6rfs.1

Fu, C. C., & Lee, L. C. (2018). Continuous monitoring of fluid and gas geochemistry for seismic study in Taiwan. Pre-Earthquake processes: A Multidisciplinary Approach to Earthquake Prediction Studies. *Geophysical Monograph Series*, *234*, 199–218. https://doi.org/10.1002/9781119156949.ch11

Fu, C. C., Mu, C. H., Kuo-Chen, H., Wang, P. L., Lin, L. H., Walia, V., et al. (2025). Geochemical characteristics and origins of CO_2 emissions within the tectonic collision boundary of the Chihshang fault, eastern Taiwan. *Geoscience Letters*, *12*(1), 23. https://doi.org/10.1186/s40562-025-00395-5

Fu, C. C., Yang, T. F., Chen, C. H., Lee, L. C., Wu, Y. M., Liu, T. K., et al. (2017). Spatial and temporal anomalies of soil gas in northern Taiwan and its tectonic and seismic implications. *Journal of Asian Earth Sciences*, *149*, 64–77. https://doi.org/10.1016/j.jseaes.2017.02.032

Fu, C. C., Yang, T. F., Du, J., Walia, V., Liu, T. K., Chen, Y. G., & Chen, C. H. (2008). Variations of helium and radon concentrations in soil gases from an active fault zone in southern Taiwan. *Radiation Measurements*, *43*, 348–352. https://doi.org/10.1016/j.radmeas.2008.03.035

Fu, C. C., Yang, T. F., Tsai, M. C., Lee, L. C., Liu, T. K., Walia, V., et al. (2017). Exploring the relationship between soil degassing and seismic activity by continuous radon monitoring in the Longitudinal Valley of eastern Taiwan. *Chemical Geology*, *469*, 163–175. https://doi.org/10.1016/j.chemgeo.2016.12.042

Fu, C. C., Yang, T. F., Walia, V., & Chen, C. H. (2005). Reconnaissance of soil gas composition over the buried fault and fracture zone in southern Taiwan. *Geochemical Journal*, *39*(5), 427–439. https://doi.org/10.2343/geochemj.39.427

Girault, F., Adhikari, L. B., France-Lanord, C., Agrinier, P., Koirala, B. P., Bhattarai, M., et al. (2018). Persistent CO_2 emissions and hydrothermal unrest following the 2015 earthquake in Nepal. *Nature Communications*, *9*(1), 2956. https://doi.org/10.1038/s41467-018-05138-z

Gulen, L., Barka, A., & Toksöz, M. N. (1987). Continental collision and related complex deformation: Maras triple junction and surrounding structures, SE Turkey. *Hacettepe University Earth Science Journal*, *14*, 319–336.

Hempton, M. R. (1987). Constraints on Arabian plate motion and extensional history of the Red Sea. *Tectonics*, *6*, 687–705. https://doi.org/10.1029/TC006i006p00687

Hoefs, J. (2009). *Stable isotope geochemistry* (6th ed.). Springer-Verlag. https://doi.org/10.1007/978-3-540-70708-0

Hu, L., Li, Y., Liu, Z., Lu, C., Martinelli, G., Yuce, G., & Du, J. (2025). Undervalued CO_2 emissions from soil to the atmosphere in seismic areas: A case study in Tangshan, North China. *Global and Planetary Change*, *249*, 104778. https://doi.org/10.1016/j.gloplacha.2025.104778

IEA. (2024). *CO_2 emissions in 2023*. IEA. Licence: CC BY 4.0 Retrieved from https://www.iea.org/reports/co2-emissions-in-2023

Inguaggiato, C., Censi, P., D'Alessandro, W., & Zuddas, P. (2016). Geochemical characterisation of gases along the dead sea rift: Evidences of mantle-CO_2 degassing. *Journal of Volcanology and Geothermal Research*, *320*, 50–57. https://doi.org/10.1016/j.jvolgeores.2016.04.008Bests

Jia, Z., Jin, Z., Marchandon, M., Ulrich, T., Gabriel, A. A., Fan, W., et al. (2023). The complex dynamics of the 2023 Kahramanmaraş, Turkey, Mw 7.8-7.7 earthquake doublet. *Science*, *381*(6661), 985–990. https://doi.org/10.1126/science.adi0685

Karabacak, V., & Altunel, E. (2013). Evolution of the northern Dead Sea fault zone in southern Turkey. *Journal of Geodynamics*, *65*, 282–291. https://doi.org/10.1016/j.jog.2012.04.012

Karabacak, V., Altunel, E., Meghraoui, M., & Akyüz, H. S. (2010). Field evidences from northern Dead Sea fault zone (South Turkey): New findings for the initiation age and slip rate. *Tectonophysics*, *480*(1–4), 172–182. https://doi.org/10.1016/j.tecto.2009.10.001

Karabulut, H., Güvercin, S. E., Hollingsworth, J., & Konca, A. O. (2023). Long silence on the East Anatolian Fault Zone (Southern Turkey) ends with devastating double earthquakes (6 February 2023) over a seismic gap: Implications for the seismic potential in the Eastern Mediterranean region. *Journal of the Geological Society*, *180*(3), jgs2023-021. https://doi.org/10.1144/jgs2023-021

Karakhanian, A. S., Trifonov, V. G., Ivanova, T. P., Avagyan, A., Rukieh, M., Minini, H., et al. (2008). Seismic deformation in the St. Simeon Monasteries (Qal'at Sim'an), Northwestern Syria. *Tectonophysics*, *453*(1–4), 122–147. https://doi.org/10.1016/j.tecto.2007.03.008

Keskin, M. (2003). Magma generation by slab steepening and breakoff beneath a subduction-accretion complex: An alternative model for collisionrelated volcanism in Eastern Anatolia, Turkey. *Geophysical Research Letters*, *30*(24), 8046. https://doi.org/10.1029/2003GL018019

Kiratzi, A. A. (1993). A study of the active crustal deformation of the North and East Anatolian fault zones. *Tectonophysics*, *225*(3), 191–203. https://doi.org/10.1016/0040-1951(93)90279-S

Kürçer, A., Domaç Yalçın, H., Elmacı, H., Özalp, S., Budakoğlu, E., Güneş, Y., et al. (2025). The 2020 Sivrice Earthquake (Mw6.8) and its seismotectonic linkage to the 2023 Kahramanmaraş Earthquakes (Mw7.8 and 7.6). (under review in Natural Hazards).

Kürçer, A., Elmacı, E., Özdemir, E., Güven, C., Güler, T., Avcu, İ., et al. (2025). The seismotectonic significance of the February 6, 2023, Pazarcık (Kahramanmaraş) earthquake (Mw 7.8) on the east Anatolian Fault Zone: In light of fault geometry, segmentation, and slip distribution data (under review in Earth-Science Reviews).

Li, J., Guo, Z., Zhang, M., Zhao, W., Dingwell, D. B., Zheng, G., et al. (2024). Deep-sourced CO_2 emissions from the Eastern Himalaya Syntaxis and the Tengchong Volcanic Field, southeast Tibet. *Chemical Geology*, *645*, 121888. https://doi.org/10.1016/j.chemgeo.2023.121888

Lin, Y. T., Rumble, D., Young, E. D., Labidi, J., Tu, T. H., Chen, J. N., et al. (2023). Diverse origins of gases from mud volcanoes and seeps in tectonically fragmented terrane. *Geochemistry, Geophysics, Geosystems*, *24*(10), e2022GC010791. https://doi.org/10.1029/2022gc010791

Liu, F. L., Zhou, X. C., Dong, J. Y., Yan, Y. C., Tian, J., Li, J. C., et al. (2023). Soil gas CO_2 emissions from active faults: A case study from the Anninghe-Zemuhe Fault, Southeastern Tibetan Plateau, China. *Frontiers of Earth Science*, *11*, 1117862. https://doi.org/10.3389/feart.2023.1117862

Liu, Z., Chen, Z., Li, Y., Zhao, Z., Sun, A., Li, J., et al. (2024). Crust uplift controls the massive emissions of ^{222}Rn and CO_2 in the Northeastern Tibetan Plateau, China. *Chemical Geology*, *663*, 122280. https://doi.org/10.1016/j.chemgeo.2024.122280

Mahmoud, S., Reilinger, R., McClusky, S., Vernant, P., & Tealeb, A. (2005). GPS evidence for northward motion of the Sinai Block: Implications for E. Mediterranean tectonics. *Earth and Planetary Science Letters*, *238*(1–2), 217–224. https://doi.org/10.1016/j.epsl.2005.06.063

McClusky, S. C., Balassanian, S., Barka, A., Ergintav, S., Georgie, I., Gurkan, O., et al. (2000). Global positioning system constraints on plate kinematics and dynamics in the eastern Mediterranean Caucasus. *Journal of Geophysical Research*, *105*(B3), 5695–5719. https://doi.org/10.1029/1999JB900351

Mishima, K., Sumino, H., Yamada, T., Ieki, S., Nagakura, N., Otono, H., & Oide, H. (2018). Accurate determination of the absolute $^{3}He/^{4}He$ ratio of a synthesized helium standard gas (helium standard of Japan, HESJ): Toward revision of the atmospheric $^{3}He/^{4}He$ ratio. *Geochemistry, Geophysics, Geosystems*, *19*(10), 3995–4005. https://doi.org/10.1029/2018GC007554

O'Nions, R. K., & Oxburgh, E. R. (1988). Helium, volatile fluxes and the development of continental crust. *Earth and Planetary Science Letters*, *90*(3), 331–347. https://doi.org/10.1016/0012-821X(88)90134-3

Över, S., Kavak, K. Ş., Bellier, O., & Özden, S. (2004). Is the Amik Basin (SE-Turkey) a triple junction area? Analyses of SPOT XS imagery and seismicity. *International Journal of Remote Sensing*, *25*(19), 3857–3872. https://doi.org/10.1080/01431160310001654437

Över, S., Özden, S., & Yılmaz, H. (2004). Late Cenozoic stress state distributions along the Karasu Valley, SE Turkey. *Tectonophysics*, *380*, 43–68. https://doi.org/10.1016/j.tecto.2003.11.011

Över, S., & Ünlügenç, U. C. (1998). Seismotectonic evidence of the Antioch triple junction and recent temporal change in Quaternary to present-day stress stage Along Hatay Region (SE-Turkey). In *3rd international geology symposium of Türkiye*. In *Proceedings book* (Vol. 98).

Ragon, T., Simons, M., Bletery, Q., Cavalié, O., & Fielding, E. (2021). Astochastic view of the 2020 Elazığ Mw6.8 earthquake (Turkey). *Geophysical Research Letters*, *48*(3), e2020GL090704. https://doi.org/10.1029/2020GL090704

Reilinger, R., McClusky, S. C., Oral, M. B., King, W., Toksöz, M. N., Barka, A. A., et al. (1997). Global positioning, system measurements of present-day crustal movements in the Arabia-Africa-Eurasia plate collision zone. *Journal of Geophysical Research*, *102*(B5), 9983–9999. https://doi.org/10.1029/96JB03736

Rojay, B., Heimann, A., & Toprak, V. (2001). Neotectonic and volcanic characteristics of the Karasu fault zone (Anatolia, Turkey): The transition zone between the Dead Sea transform and the East Anatolian fault zone. *Geodinamica Acta*, *14*(1–3), 197–212. https://doi.org/10.1080/09853111.2001.11432444

Sano, Y., & Wakita, H. (1985). Geographical distribution of $^{3}He/^{4}He$ ratios in Japan: Implications for arc tectonics and incipient magmatism. *Journal of Geophysical Research*, *90*(B10), 8729–8741. https://doi.org/10.1029/JB090iB10p08729

Sano, Y., & Marty, B. (1995). Origin of carbon in fumarolic gas from island arcs. *Chemical Geology*, *119*(1–4), 265–274. https://doi.org/10.1016/0009-2541(94)00097-R

Sano, Y., Tokutake, T., & Takahata, N. (2008). Accurate measurement of atmospheric helium isotopes. *Analytical Sciences*, *24*(4), 521–525. https://doi.org/10.2116/analsci.24.521

Sano, Y., Tominaga, T., Nakamura, Y., & Wakita, H. (1982). $^{3}He/^{4}He$ ratios of methane-rich natural gases in Japan. *Geochemical Journal*, *16*(5), 237–245. https://doi.org/10.2343/geochemj.16.237

Saroglu, F., Emre, O., & Kuşçu, I. (1992). The East Anatolian fault zone of Turkey. *Annales Tectonicae*, *6*, 99–125.

Sengör, A. M. C., & Yilmaz, Y. (1981). Tethyan evolution of Turkey: A plate tectonic approach. *Tectonophysics*, *75*(3–4), 181–241. https://doi.org/10.1016/0040-1951(81)90275-4

Sensintaffar, E. L., & Windham, S. T. (1990). Calibration of scintillation cells for radon-222 measurements at the U.S. Environmental Protection Agency. *Journal of Research of the National Institute of Standards and Technology*, *95*(2), 143–145. https://doi.org/10.6028/jres.095.016

Seyrek, A., Demir, T., Pringle, M., Yurtmen, S., Westaway, R., Beck, A., & Rowbotham, G. (2007). Kinematics of the Amanos Fault, southern Turkey, from Ar-Ar dating of offset Pleistocene basalt flows: Transpression between the African and Arabian plates. In W. D. Cunningham & P. Mann (Eds.), *Tectonics of strike-slip restraining and releasing bends* (Vol. 290, pp. 255–284). Geological Society Special Publication.

Sieh, K. E., Stuiver, M., & Brillinger, D. (1989). A more precise chronology of earthquakes produced by the San Andreas Fault in southern California. *Journal of Geophysical Research*, *94*(B1), 603–623. https://doi.org/10.1029/JB094iB01p00603

Sinclair, A. J. (1974). Selection of threshold values in geochemical data using probability graphs. *Journal of Geochemical Exploration*, *3*(2), 129–149. https://doi.org/10.1016/0375-6742(74)90030-2

Smith, S. P., & Kennedy, B. M. (1983). The solubility of noble gases in water and NaCl brine. *Geochimica et Cosmochimica Acta*, *47*(3), 503–515. https://doi.org/10.1016/0016-7037(83)90273-9

Sunbul, F. (2019). Time-dependent stress increase along the major faults in eastern Turkey. *Journal of Geodynamics*, *126*, 23–31. https://doi.org/10.1016/j.jog.2019.03.001

Taftsoglou, M., Valkaniotis, S., Papathanassiou, G., & Karantanellis, E. (2023). Satellite imagery for rapid detection of liquefaction surface manifestations: The case study of Türkiye-Syria 2023 Earthquakes. *Remote Sensing*, *15*(17), 4190. https://doi.org/10.3390/rs15174190

Tari, U., Tüysüz, O., Gençe, Ş. C., İmren, C., Blackwell, B. A. B., Lom, N., et al. (2013). The geology and morphology of the Antakya graben between the Amik triple junction and the Cyprus Arc. *Geodinamica Acta*, *26*(1–2), 27–55. https://doi.org/10.1080/09853111.2013.858962

Tatar, O., Piper, J. D. A., Gürsoy, H., Heimann, A., & Koçbulut, F. (2004). Neotectonic deformation in the transition zone between the Dead Sea Transform and the East Anatolian Fault Zone, southern Turkey: A palaeomagnetic study of the Karasu Rift volcanism. *Tectonophysics*, *385*(1–4), 17–43. https://doi.org/10.1016/j.tecto.2004.04.005

Torfstein, A., Hammerschmidt, K., Friedrichsen, H., Starinsky, A., Garfunkel, Z., & Kolodny, Y. (2013). Helium isotopes in Dead Sea transform waters. *Chemical Geology*, *352*, 188–201. https://doi.org/10.1016/j.chemgeo.2013.06.008

Walia, V., Lin, S. J., Fu, C. C., Yang, T. F., Hong, W. L., Wen, K. L., & Chen, C. H. (2010). Soil-gas monitoring: A tool for fault delineation studies along Hsinhua Fault (Tainan), southern Taiwan. *Applied Geochemistry*, *25*(4), 602–607. https://doi.org/10.1016/j.apgeochem.2010.01.017

Walia, V., Su, T. C., Fu, C. C., & Yang, T. F. (2005). Spatial variations of radon and heliumconcentration in soil gas across Shan-Chiao fault, Northern Taiwan. *Radiation Measurements*, *40*(2–6), 513–516. https://doi.org/10.1016/j.radmeas.2005.04.011

Walia, V., Yang, T. F., Lin, S. J., Kumar, A., Fu, C. C., Chiu, J. M., et al. (2013). Temporal variation of soil gas compositions for earthquake surveillance in Taiwan. *Radiation Measurements*, *50*, 154–159. https://doi.org/10.1016/j.radmeas.2012.11.007

Wang, J., Liu, C., Chen, Z., Zhang, Z., Zhang, F., & Zhang, S. (2024). Geochemical characterization and implications of soil gas and geothermal fluids in the fault zone of Xiongan new area. *Applied Geochemistry*, *161*, 105886. https://doi.org/10.1016/j.apgeochem.2023.105886

Wang, Y., Zhou, X., Tian, J., Zhou, J., He, M., Li, J., et al. (2023). Volatile characteristics and fluxes of He-CO_2 systematics in the southeastern Tibetan Plateau: Constraints on regional seismic activities. *Journal of Hydrology*, *617*(Part C), 129042. https://doi.org/10.1016/j.jhydrol.2022.129042

Yang, T. F., Chou, C. Y., Chen, C. H., Chyi, L. L., & Jiang, J. H. (2003). Exhalation of radon and its carrier gases in SW Taiwan. *Radiation Measurements*, *36*(1–6), 425–429. https://doi.org/10.1016/S1350-4487(03)00164-1

Yang, T. F., Fu, C. C., Walia, V., Chen, C. H., Chyi, L. L., Liu, T. K., et al. (2006). Seismo-geochemical variations in SW Taiwan: Multi-parameter automatic gas monitoring results. *Pure and Applied Geophysics*, *163*(4), 693–709. https://doi.org/10.1007/s00024-006-0040-3

Yang, T. F., Lan, T. F., Lee, H. F., Fu, C. C., Chuang, P. C., Lo, C. H., et al. (2005). Gas compositions and helium isotopic ratios of fluid samples around Kueishantao, NE offshore Taiwan and its tectonic implications. *Geochemical Journal*, *39*(5), 469–480. https://doi.org/10.2343/geochemj.39.469

Yuce, G., Fu, C. C., D'Alessandro, W., Gulbay, A. H., Lai, C. W., Bellomo, S., et al. (2017). Geochemical characteristics of soil radon and carbon dioxide within the Dead Sea Fault and Karasu Fault in the Amik Basin (Hatay). Turkey. *Chemical Geology*, *469*, 129–146. https://doi.org/10.1016/j.chemgeo.2017.01.003

Yuce, G., Italiano, F., D'Alessandro, W., Yalcin, T. H., Yasin, D. U., Gulbay, A. H., et al. (2014). Origin and interactions of fluids circulating over the Amik Basin (Hatay-Turkey) and relationships with the hydrologic, geologic and tectonic settings. *Chemical Geology*, *388*, 23–39. https://doi.org/10.1016/j.chemgeo.2014.09.006

Yürür, M. T., & Chorowicz, J. (1998). Recent volcanism, tectonics and plate kinematics near the junction of the African, Arabian and Anatolian Plates in the Eastern Mediterranean. *Journal of Volcanology and Geothermal Research*, *85*(1–4), 1–15. https://doi.org/10.1016/S0377-0273(98)00046-8

Erratum

The originally published version of this article contained a typographical error. Coauthor Ş. Gürboğa's name was incorrectly presented as Ş.D Gürboğa. The error has been corrected, and this may be considered the authoritative version of record.